



Asymmetry in the Q_y Fluorescence and Absorption Spectra of Chlorophyll *a* Pertaining to Exciton Dynamics

Jeffrey R. Reimers¹, Margus Rätsep² and Arvi Freiberg^{2,3*}

¹ School of Chemistry, The University of Sydney, Sydney, NSW, Australia, ² Institute of Physics, University of Tartu, Tartu, Estonia, ³ Institute of Molecular and Cell Biology, University of Tartu, Tartu, Estonia

OPEN ACCESS

Edited by:

Doran Bennett,
Southern Methodist University,
United States

Reviewed by:

Hui Li,
Jilin University, China
Tim Zuehlsdorff,
Oregon State University, United States

*Correspondence:

Arvi Freiberg
arvi.freiberg@ut.ee

Specialty section:

This article was submitted to
Physical Chemistry and Chemical
Physics,
a section of the journal
Frontiers in Chemistry

Received: 28 July 2020

Accepted: 26 October 2020

Published: 02 December 2020

Citation:

Reimers JR, Rätsep M and Freiberg A
(2020) Asymmetry in the Q_y
Fluorescence and Absorption Spectra
of Chlorophyll *a* Pertaining to Exciton
Dynamics. *Front. Chem.* 8:588289.
doi: 10.3389/fchem.2020.588289

Significant asymmetry found between the high-resolution Q_y emission and absorption spectra of chlorophyll-*a* is herein explained, providing basic information needed to understand photosynthetic exciton transport and photochemical reactions. The Q_y spectral asymmetry in chlorophyll has previously been masked by interference in absorption from the nearby Q_x transition, but this effect has recently been removed using extensive quantum spectral simulations or else by analytical inversion of absorption and magnetic circular dichroism data, allowing high-resolution absorption information to be accurately determined from fluorescence-excitation spectra. To compliment this, here, we measure and thoroughly analyze the high-resolution differential fluorescence line narrowing spectra of chlorophyll-*a* in trimethylamine and in 1-propanol. The results show that vibrational frequencies often change little between absorption and emission, yet large changes in line intensities are found, this effect also being strongly solvent dependent. Among other effects, the analysis in terms of four basic patterns of Duschinsky-rotation matrix elements, obtained using CAM-B3LYP calculations, predicts that a chlorophyll-*a* molecule excited into a specific vibrational level, may, without phase loss or energy relaxation, reemit the light over a spectral bandwidth exceeding $1,000\text{ cm}^{-1}$ (0.13 eV) to influence exciton-transport dynamics.

Keywords: absorption-emission asymmetry, differential fluorescence line narrowing, coherent energy redistribution, exciton transport, photosynthesis, density functional theory, Duschinsky rotation

INTRODUCTION

Chlorophyll-*a* (Chl-*a*) is the most common chlorophyllide utilized in natural photosynthesis (van Grondelle et al., 1994; Blankenship et al., 2004; Grimm et al., 2006; Laisk et al., 2009). For all processes in which this molecule is involved, including light capture, coherent and incoherent exciton transport, and charge transport, the dissipation of energy (the reorganization energy λ) through intramolecular nuclear relaxation is a critical process (Hush, 1958; May and Kühn, 2008). Critical for exciton transport are both the ground-state reorganization energy λ^E and excited-state reorganization energy λ^A , which can be measured and partitioned into individual vibrational

components using modern high-resolution techniques (Rebane and Avarmaa, 1982; Avarmaa and Rebane, 1985; Jaaniso and Avarmaa, 1986; Renge et al., 1987; Sild and Haller, 1988; Gillie et al., 1989; den Hartog et al., 1998; Rätsep et al., 1998, 2009a, 2011, 2019b; Zazubovich et al., 2001; Rätsep and Freiberg, 2003; Hughes et al., 2004; Purchase and Völker, 2009; Jankowiak et al., 2011; Pieper and Freiberg, 2014; Adolphs et al., 2016; Leiger et al., 2017). For excited-state properties, hole-burning techniques are commonly applied, but there are still ambiguities in the baseline limit quantitative analysis, with fluorescence-excitation being a more robust technique provided that the contribution from the zero-phonon line (ZPL) can be determined by other means (Reimers et al., 2013; Pieper et al., 2018). For ground-state vibrations, only relatively recently has the differential fluorescence line-narrowing techniques (Δ FLN) (Rätsep and Freiberg, 2003, 2007; Rätsep et al., 2009a, 2019a) been developed to deliver similar results. These techniques provide critical vibrational data required for studies of, e.g., coherent energy transport in photosystems (Renger et al., 1996; Huo and Coker, 2010; Rivera et al., 2013; Kreisbeck et al., 2014; Müh et al., 2014; Romero et al., 2014; Malý et al., 2016; Duan et al., 2017; Ren et al., 2018; Cao et al., 2020; Tomasi and Kassal, 2020).

It is very convenient in quantum dynamics calculations of energy and/or electron transport to assume that the reorganization energy has the same value and the same distribution amongst normal modes on both the ground and excited state (Rebane, 1970). In this situation, both low-resolution and high-resolution absorption and emission spectra are symmetric, i.e., after appropriate normalization and reflection of (say) the emission spectrum about its origin, the two spectra are identical. The observed low-resolution spectra for Chl-a (Rätsep et al., 2009a), bacteriochlorophyll-a (BChl-a) (Rätsep et al., 2011), and pheophytin-a (Pheo-a) (Rätsep et al., 2019b) are significantly asymmetric. Various explanations of this could be envisaged suggestive that quantum dynamics calculations performed assuming symmetry should give realistic results: the vibrational frequency of some key modes could be different in the ground and excited states, or the most intense lines in absorption and emission could be of the same nature, with just their intensities modulated. Nevertheless, the observation of high-resolution data showed that such scenarios do not apply: many of the intense modes in either absorption or emission are just not seen at all in the other spectrum (Rätsep et al., 2011, 2019b), suggesting the possibility of serious failure for symmetry-based quantum dynamics models for exciton transfer. As before, only through the measurement of both high-resolution absorption and emission spectra can the implications of this for quantum dynamics be made apparent. Of important note, the asymmetry is shown to be environment-dependent (Rätsep et al., 2011, 2019b), allowing, in principle, metal chelation and changes to nearby residues and solvent location to modulate transport in a protein environment.

For Chl-a, BChl-a, and Pheo-a, the lowest-energy excited state is Q_y and the next state is Q_x (Gouterman et al., 1963). For Chl-a, a critical qualitative feature contributing to absorption-emission asymmetry is that the Q_x - Q_y energy spacing is small, resulting in overlapping absorptions. Indeed, the nature of Q_x and its spectral impact had been debated for over 50 years,

with all issues being resolved in 2013 using a model involving strong resonant non-adiabatic coupling mixing the natures of the Q_x and Q_y states (Reimers et al., 2013). Non-adiabatic coupling splits the absorption intensity of the Q_x state into two separate spectral regions, the lower-energy component centered around a strongly perturbed Q_y vibrational mode in the region of the Q_y origin plus 300–1,000 cm^{-1} , with the higher-energy component placed 1,000–1,300 cm^{-1} further away. Before this assignment was established, it was hypothesized that just one of the two resolved component bands depicted Q_x , leading to two competitive assignments based upon the chosen component. Neither of the assignments could account for all observed (and calculated) data, leading to the extended debate. That strong non-adiabatic coupling dominates the spectral properties is a rather unusual situation in molecular spectroscopy. As a result, no approach based on the Born-Oppenheimer approximation (Huang Rhys factors, Herzberg-Teller couplings, etc.) can account for the observed spectra properties. In particular, the Q_x origin transition energy, as perceived by quantum-chemical calculations, pertains to a region of *minimal* absorption *between* the two observed x -polarized spectral peaks. Nevertheless, the naïve assignment of Q_x to one of the two observed peaks still remains common practice (Sirohiwal et al., 2020), resulting in serious overestimation of the observed Q_x - Q_y spacing.

Despite the complexity of observed absorption spectra owing to the strong Q_x - Q_y non-adiabatic interaction, a simple interpretation of the observed spectral properties is still possible (Reimers et al., 2013). Details pertaining to the location, width, and intensity of each of the two x -polarized absorption components can be understood in terms of one parameter: the energy difference ΔE between the Q_x and Q_y states. This is controlled by the magnesium coordination, as well as external environmental influences (Reimers et al., 2013). In gas-phase complexes, and 5-coordinate solvents and most protein environments, the x -polarized absorption becomes hidden underneath the strong Chl-a Franck-Condon 0–1 vibrational sideband centered at the origin plus $\sim 1,300 \text{ cm}^{-1}$. However, in 6-coordinate environments, this component moves into a sparser spectral region at about half this spacing and, hence, often becomes clearly resolved.

Understanding the breakdown of the Born-Oppenheimer approximation for Chl-a is critical to any quantitative analysis pertaining to both low-resolution and high-resolution absorption spectra. It allows the observed (Avarmaa and Rebane, 1985) high-resolution fluorescence-excitation spectra to be separated into broad underlying contributions associated with Q_x , as well as high-resolution features depicting the intrinsic nature of Q_y (Reimers et al., 2013). This has led to the first quantitative high-resolution description of Q_y absorption. Details of the non-adiabatic coupling between Q_y and Q_x in chlorophyllides have also been studied recently using two-dimensional spectroscopies (Bukarte et al., 2020), revealing properties critical to function. Ultrafast relaxation of light energy absorbed with x -polarization to energy emitted with y -polarization is controlled largely by ΔE (Reimers et al., 2013).

To investigate the absorption-emission asymmetry of Chl-a in high resolution, what therefore remains is the measurement and interpretation of its high-resolution emission

spectrum. Herein, we measure and analyze the Q_y emission spectra of Chl-a using the Δ FLN technique in two different solvents: trimethylamine (TEA) and 1-propanol. The identified asymmetry in combination with low-resolution absorption-emission spectra is then interpreted based on the results of density-functional theory (DFT) simulation of the electronic and nuclear structures. A self-consistent set of spectroscopic approximations is used in both the experimental data analysis and in the interpretation of the DFT simulations.

All calculations reported in the main text are performed in the gas phase. Treatments of solvent through implicit and/or explicit methods can be very successful (Hush and Reimers, 2000; Tomasi, 2011; Mennucci, 2012; Skyner et al., 2015; Zuehlsdorff and Isborn, 2018; Caricato, 2019; Cerezo et al., 2020), but no such approach has been demonstrated as yet to be successful for understanding chlorophyll bandshapes. Indeed, results presented in **Supplementary Table 1** using commonly applied solvation treatments fail to provide qualitatively useful information, as has been previously noted for bacteriochlorophyll-a (Higashi et al., 2014). Spectra of Chl-a complexes have been recorded in the gas phase (Shafizadeh et al., 2011; Kjær et al., 2020), but as yet no high-resolution information is available. We demonstrate that use of gas-phase calculations allows for the key qualitative features that control absorption-emission asymmetry in Chl-a to be identified. In this process, a map is created that shows how the most important high-resolution vibrational lines observed in absorption-type experiments relate to those observed in emission-type experiments.

METHODS

Sample Preparation and Spectral Measurements

Chl-a powder purchased from Sigma-Aldrich was stored in the dark at -18°C before dissolving in high-grade solvents of 1-propanol and TEA. Plastic (polymethyl methacrylate) cuvettes of 5 mm path length were used as sample containers. Pigment concentrations below 4×10^{-6} M were used in fluorescence measurements, providing optical densities <0.05 at the Q_y absorption maximum. This low concentration of Chl-a largely eliminated aggregation and self-absorption effects.

Absorption and fluorescence measurements were made using an experimental setup that has been previously described (Rätsep et al., 2009a, 2019a). It consists of a Andor Shamrock 0.3 m spectrograph equipped with a thermo-electrically cooled CCD camera, a highly stabilized tungsten light source, and a He bath cryostat. Selective excitation of fluorescence was performed using a model 375 dye laser of <0.5 cm^{-1} linewidth, pumped by a Spectra Physics Millennia solid state laser. The inhomogeneous spectral resolution of the measurements was 6.6 cm^{-1} .

Dipole Strength Representation of the Observed Spectra

Absorption and emission band strengths were obtained from raw observed spectra through the application of appropriate frequency scaling. Absorption spectra were scaled by ν^{-1} while

emission spectra were scaled by ν^{-3} , as absorption and emission strengths are proportional to νM^2 and $\nu^3 M^2$, respectively, where $M^2 \equiv I$ is the band strength (Einstein, 1916) and ν is the absorption frequency. As all emission spectra were recorded linearly in wavelength, the total scaling of the emission spectra used was ν^{-5} , with the additional factor of ν^{-2} required so as to preserve the integrated emission probability.

Vibrational Structure of the Spectra

In the Huang-Rhys approximation (Huang et al., 1950), the relative band strength of the $0-n_i$ transition delivering n_i quanta into vibrational mode i is given by the Poisson distribution

$$I_i = e^{-S_i} S_i^{n_i} / n_i! \quad (1)$$

where S_i is the Huang-Rhys factor for mode i . The relative band strength of the transitions from the zero-point level of one state to an arbitrary level $n \equiv \{n_1, n_2, \dots, n_i, \dots\}$ of the other state compared to that of the origin line strength, I_{00} , is given by

$$\frac{I_n}{I_{00}} = \prod_i \frac{S_i^{n_i}}{n_i!} \quad (2)$$

which reduces to

$$\frac{I_i}{I_{00}} = S_i \quad (3)$$

for the $0-1$ transition in mode i . The total Huang-Rhys factor for the electronic transition is thus given as

$$S_{vib} = \sum_i S_i = \frac{1}{I_{00}} \sum_i I_i = \frac{I_{vib}}{I_{00}} \quad (4)$$

where I_{vib} is the total band strength attributable to $0-1$ transitions, and the total band strength is decomposed as

$$I_{tot} = I_{00} + I_{vib} + I_{mq} \quad (5)$$

where I_{mq} is the component attributable to multi-quanta (i.e., $\sum_i n_i > 1$) transitions. The reorganization energy distributed by each mode is given by

$$\lambda_i = h\nu_i S_i \quad (6)$$

and the total reorganization energy by.

$$\lambda = \sum_i \lambda_i. \quad (7)$$

DFT Calculations

Ground and Q_y excited-state optimized structures for Chl-a, modified with methyl replacing phytol, are evaluated by the CAM-B3LYP (Yanai et al., 2004), MN15 (Yu et al., 2016), ω B97xD (Chai and Head-Gordon, 2008), and B3LYP (Becke, 1993) methods using Gaussian-16 (Frisch et al., 2016) with the 6-31G* basis set (Hehre et al., 1972). Replacement of phytol with methyl is not expected to have noticeable influences on the properties of interest herein, although its replacement with H

(making a carboxylic acid) can be influential (Fiedor et al., 2003, 2008; Palm et al., 2019). Also, the choice of basis set has a small influence (Rätsep et al., 2011), but as this is much less than the effect of solvent variation, it is not pursued herein. As was already mentioned in the introduction, only gas-phase calculations are reported in the main text, but in the **Supplementary Material** results are presented using both implicit solvation, applying the polarizable-continuum model (PCM) (Tomasi et al., 2005), and/or explicit solvation. All such calculations include the D3(BJ) dispersion correction (Goerigk and Grimme, 2011).

The normal modes for both states are determined analytically and projected onto curvilinear coordinates using the DUSHIN program (Reimers, 2001). This approach expresses the geometry changes calculated by the various methods between the ground and excited states in terms of bond-length, bond-angle, and bond-torsion changes, these then being projected onto ground- and excited-state normal coordinates evaluated by Gaussian-16. The force-constant matrix after transformation to these redundant internal coordinates (Wilson et al., 1955) may optionally be scaled by factors of 0.95, 0.95, and 0.99 for the stretching, bending, and torsional motions, respectively. These factors were previously obtained by fitting the observed and CAM-B3LYP/6-31G* calculated vibrational frequencies of free-base porphyrin for all modes except the CH and NH stretches (Rätsep et al., 2011).

RESULTS AND DISCUSSION

Interpretation of Low-Resolution and High-Resolution Spectra

The observed low-resolution and high-resolution (Δ FLN) fluorescence spectra of Chl-a in solid matrices of TEA and 1-propanol at 4.5 K are shown in **Figure 1**. The low-resolution fluorescence spectra were obtained following non-resonant excitation at 407 nm and are broad; in contrast, the resonantly excited Δ FLN spectra demonstrate a clear-cut vibrational structure, demonstrating the significant advantages of this technique. According to Equation (5), the Δ FLN spectrum displays an origin band that comprises the ZPL and PSB components, with intertwined $I_{\text{vib}} + I_{\text{mq}}$ vibrational sidebands extending toward longer wavelengths. The shape of the origin band $I_{00}(\nu)$ is known to depend on the excitation wavelength, with significant variations observed even for small changes within the inhomogeneous spread of ZPL frequencies, showing enhancement of the electron-phonon coupling strength with increasing transition wavelength (Rätsep et al., 2009b; Renge et al., 2011). Comparing the low-resolution spectra obtained in different environments, one may conclude that the vibrational sideband is more intense in 1-propanol than in TEA, details of which are revealed by the Δ FLN spectra. These important variances will be in detail elaborated below.

Figure 2 shows the vibrational parts of the Δ FLN spectra, presented as a function of the frequency difference $\Delta\nu$ from the ZPL maximum. These are displayed with their identified origin band profiles $I_{00}(\nu)$ subtracted to enhance clarity in the

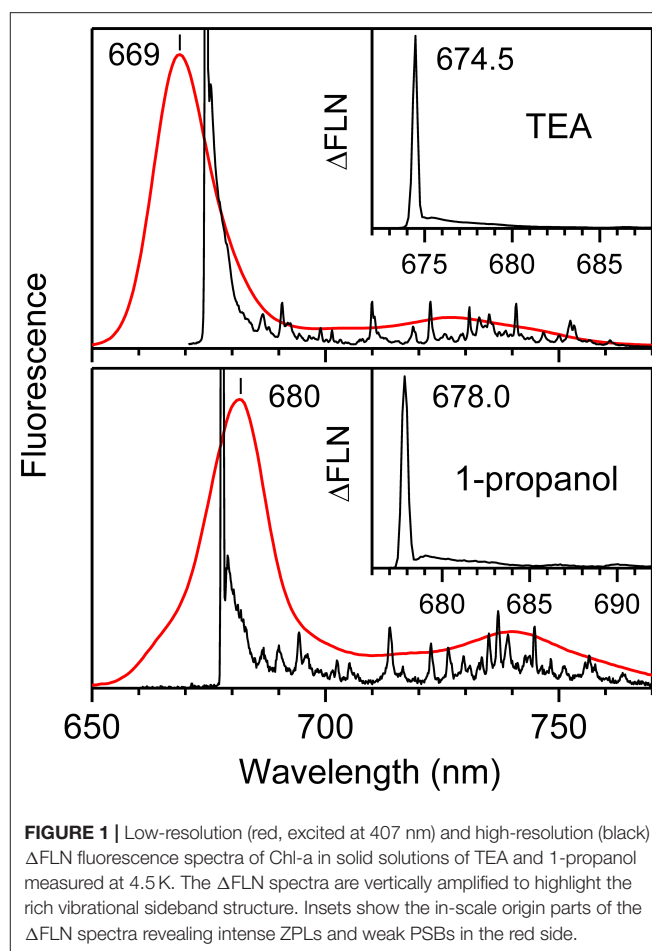


FIGURE 1 | Low-resolution (red, excited at 407 nm) and high-resolution (black) Δ FLN fluorescence spectra of Chl-a in solid solutions of TEA and 1-propanol measured at 4.5 K. The Δ FLN spectra are vertically amplified to highlight the rich vibrational sideband structure. Insets show the in-scale origin parts of the Δ FLN spectra revealing intense ZPLs and weak PSBs in the red side.

low-frequency region up to about 600 cm^{-1} . The $I_{00}(\nu)$ profiles, shown in green in the main figures and their insets, are expressed as a sum of two contributions: a Gaussian ZPL function fitted to an observed resolution of 6.6 cm^{-1} and a phonon side band (PSB) fitted to a standard form (Pajusalu et al., 2014).

In **Figure 3**, the two Δ FLN spectra are overlaid to facilitate detailed comparison: most lines appear to share common frequencies, with in only a few cases frequency shifts being apparent that are most likely associated with specific solvation effects. In contrast, it is clear that the intensity patterns change significantly. Hence, vibrational frequencies are mostly insensitive to the environment, whereas the associated intensities, which depend on the details of the vibrational motions, are very sensitive.

For quantitative evaluation, the observed Δ FLN spectra were fitted with Equation (5), using a model containing 215 vibrational modes for Chl-a in 1-propanol and 296 models for Chl-a in TEA. For the spectrum in TEA, this was done using a fully automated procedure in which all frequency intervals were set to be less than the spectral resolution of the measurement, whereas for the 1-propanol spectrum, the frequencies were optimized to create a model containing the fewest-possible number of modes. These two approaches, full automation and human perceptive intuition,

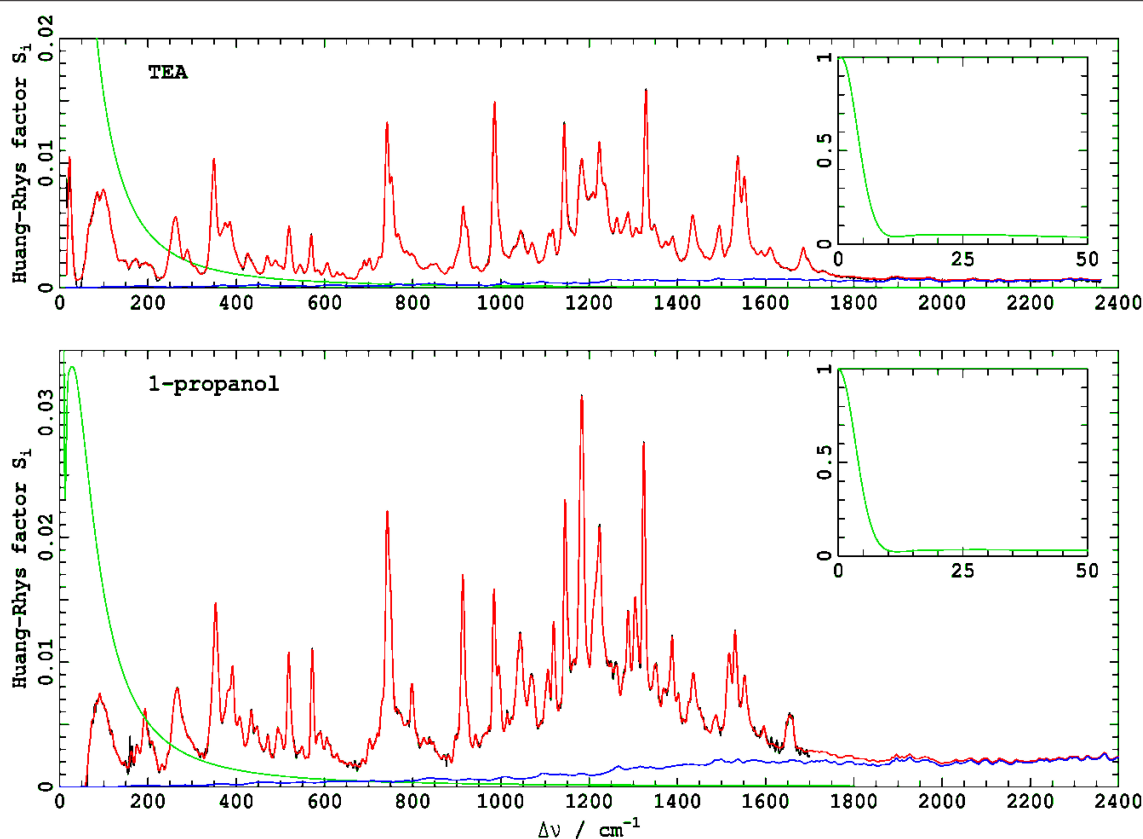


FIGURE 2 | Vibrational parts of the Δ FLN spectra of Chl-a in TEA and 1-propanol recorded at 4.5 K. The green curves, shown on a different scale in the insets, indicate origin band profiles $I_{00}(\nu)$ that are subtracted from experimental Δ FLN spectra to enhance clarity in the low-frequency region. The Huang-Rhys model fits (red) to the experimental vibrational contribution (black) was performed with the lineshape of every vibrational transition set to that observed for the 0–0 line, $I_{00}(\nu)$. Contributions to the fit arising from multi-quanta transitions are shown in blue. The spectra are normalized to give a peak height of the 0–0 line of unity, allowing the Huang-Rhys factor S_i for any non-overlapped 0–1 transition to be read off the y axis from its peak height. The $I_{00}(\nu)$ profiles (green) are expressed as a sum of two contributions: a Gaussian ZPL fitted to an observed resolution of 6.6 cm^{-1} and a PSB fitted to a standard form (Pajusalu et al., 2014).

yield results of similar quality and usefulness. In both cases, the associated Huang-Rhys factors S_i were optimized to minimize the difference between the observed and fitted spectra. By using $I_{00}(\nu)$ as the profile for each and every vibrational line (Rebane, 1970), the fundamental and multi-quanta contributions $I_{vib}(\nu) + I_{mq}(\nu)$ were determined simultaneously during the fitting.

In **Figure 2**, the fitted spectra in red are overlaid on top of the observed spectra shown in black. That very little black color can be seen in the figures is indicative of the very high quality of the fitted results. Contributions to the spectra from multi-quanta excitations $I_{mq}(\nu)$ indicated in blue are small yet significant to the quantitative analysis. Note that, in these figures, the y-axis is labeled as “Huang-Rhys factor S_i ,” reflecting traditional analysis methods. If a 0–1 vibrational line is isolated from all others, then the height of the line in this presentation is its Huang-Rhys factor. However, as the shape of each line is taken to be $I_{00}(\nu)$, both presented spectra embody strong line overlap and hence interpretation of line data in this way is qualitatively indicative but not quantitatively accurate.

The obtained $\{v_i, S_i\}$ data sets provide a quantitative description of the observed spectra and can qualitatively be

partitioned into regions associated with resolved spectral peaks and diffuse background regions. The present data could be partitioned into 44 regions/blocks for 1-propanol and 72 regions for TEA, with each region identified with some particular resolved emission (see **Tables 1, 2** as well as the related **Supplementary Tables 4, 5**, respectively). This partitioning was done so as to preserve the originally fitted total reorganization energy within each region, with an effective Huang-Rhys factor determined to suit. This results in reduced region-based data sets $\{v_j, S_j\}$ defined with

$$\lambda_j = \sum_i^{\text{region } j} \lambda_i, \quad S_j = \frac{1}{v_{\max,j}} \lambda_j, \quad (8)$$

where $v_{\max,j}$ is the frequency of the identified peak in region j . In this way, the background signal, which provides a substantial fraction to the whole, is accumulated to its embodied Δ FLN peak. The resulting description, therefore, achieves simplicity whilst retaining key features required in, e.g., quantum simulations of exciton transport. Further similar simplifications retaining just

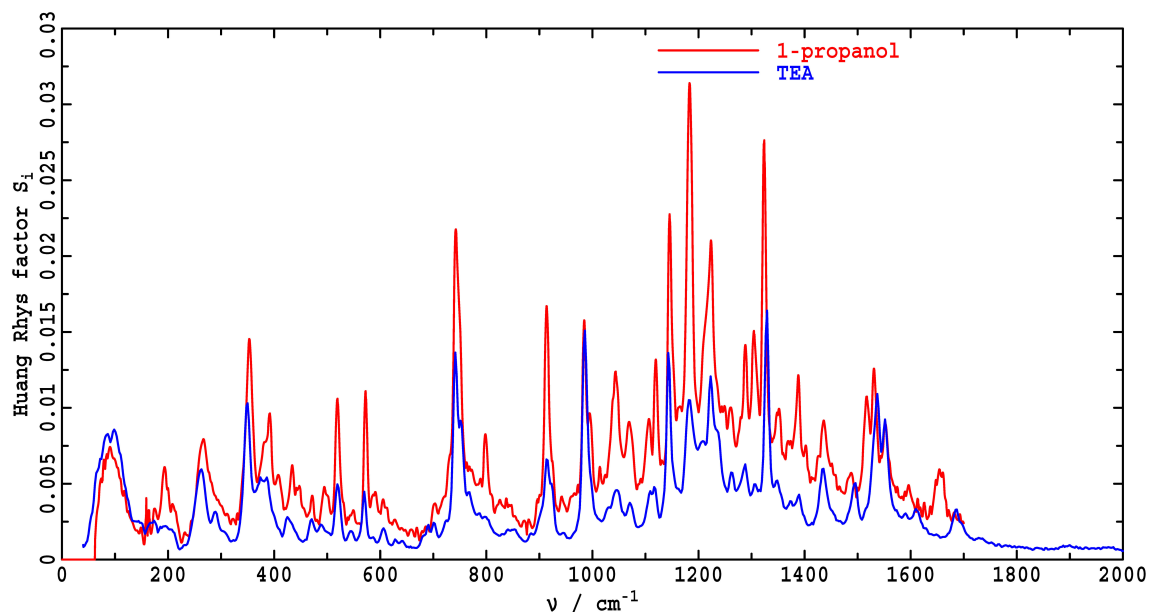


FIGURE 3 | Comparison of vibrational parts of the Δ FLN spectra of Chl-a in 1-propanol and TEA recorded at 4.5 K. The y-scale is such that the value of the Huang-Rhys factor for a vibrational fundamental that is not overlapped by other peaks is given by the peak height, see text for further details.

TABLE 1 | Resolved component regions j fitted according to Equation (8) in **Supplementary Table 5** to the observed Δ FLN spectrum of Chl-a in 1-propanol at 4.5 K, depicting the component peak frequencies ν_j (cm^{-1}), the range of individual frequencies included in each region (cm^{-1}), the net emission reorganization energy λ_j^E (cm^{-1}) for each region, and the effective emission Huang-Rhys factor S_j^E required to reproduce this.

ν_j	Range	$1,000 S_j^E$	λ_j^E	ν_j	Range	$1,000 S_j^E$	λ_j^E
92 ^a	66–151	41.2	3.8	985	958–1,008	31.7	31.2
194	157–210	16.5	3.2	1,016	1,015	3.0	3.0
267	218–315	33.1	8.8	1,043	1,023–1,049	23.8	24.8
353	322–366	30.6	10.8	1,064	1,055–1,080	16.5	17.5
380	372–379	7.1	2.7	1,107	1,086–1,107	11.5	12.7
392	385–392	11.1	4.3	1,120	1,113–1,135	16.3	18.3
408	400–414	7.0	2.9	1,146	1,145–1,167	36.3	41.6
434	422–435	5.9	2.6	1,183	1,174–1,192	46.8	55.4
448	442–456	5.2	2.3	1,224	1,198–1,250	55.9	68.5
472	463–479	3.3	1.6	1,261	1,258–1,271	7.8	9.9
495	487–502	6.0	3.0	1,288	1,277–1,289	13.5	17.5
519	510–541	14.3	7.4	1,306	1,296–1,311	18.1	23.6
549	549–560	2.2	1.2	1,324	1,317–1,339	29.5	39.1
573	573–584	11.8	6.8	1,352	1,347–1,359	8.5	11.5
591	592	2.5	1.5	1,374	1,368–1,381	7.4	10.1
606	599–613	4.3	2.6	1,388	1,388–1,395	8.6	12.0
664	620–697	5.7	3.8	1,402	1,403	2.8	4.0
703	703	2.2	1.6	1,436	1,414–1,465	15.7	22.6
743	712–755	47.7	35.5	1,488	1,471–1,495	3.8	5.6
763	763–775	8.0	6.1	1,517	1,502–1,521	12.0	18.3
798	782–805	11.2	8.9	1,531	1,525–1,536	11.4	17.5
838	810–882	8.4	7.1	1,552	1,542–1,585	11.0	17.0
914	903–933	27.5	25.1	1,596	1,596	1.2	1.9
942	942–951	2.7	2.6	1,654	1,648–1,661	6.3	10.4
Total						715	650

^aIt is unclear as to whether all or part of this emission should be attributed to intramolecular vibrations, as reported in this table and elsewhere, or else to intermolecular phonons.

TABLE 2 | Resolved component regions j fitted according to Equation (8) in **Supplementary Table 6** to the observed Δ FLN spectrum of Chl-a in TEA at 4.5 K, depicting the component peak frequencies ν_j (cm^{-1}), the range of individual frequencies included in each region (cm^{-1}), the net emission reorganization energy λ_j^E (cm^{-1}) for each region, and the effective emission Huang-Rhys factor S_j^E required to reproduce this.

ν_j	Range	1,000 S_j^E	λ_j^E	ν_j	Range	1,000 S_j^E	λ_j^E
22	10–41	13.1	0.3	1,032	1,018–1,036	2.8	2.9
66	41–87	20.1	1.3	1,046	1,036–1,060	6.2	6.5
99	87–115	20.3	2.0	1,071	1,060–1,090	4.5	4.8
123	115–155	4.2	0.5	1,109	1,090–1,113	4.8	5.4
174	155–190	3.3	0.6	1,117	1,113–1,127	4.2	4.7
206	190–220	2.4	0.5	1,144	1,127–1,150	15.9	18.2
263	220–280	14.6	3.8	1,157	1,150–1,170	6.3	7.3
289	280–312	4.5	1.3	1,183	1,170–1,192	15.2	18.0
330	312–335	1.1	0.4	1,209	1,192–1,213	14.0	16.9
349	335–362	17.3	6.0	1,223	1,213–1,229	13.6	16.6
375	362–380	7.0	2.6	1,236	1,229–1,242	7.5	9.3
386	380–412	6.7	2.6	1,263	1,242–1,272	5.9	7.5
425	412–432	1.6	0.7	1,275	1,272–1,283	2.9	3.7
436	432–458	1.0	0.5	1,288	1,283–1,301	5.7	7.4
471	458–477	2.2	1.1	1,306	1,301–1,311	2.7	3.6
489	477–500	3.1	1.5	1,315	1,311–1,320	2.0	2.7
520	500–530	7.0	3.6	1,329	1,320–1,335	17.0	22.5
545	530–558	1.5	0.8	1,342	1,335–1,347	3.1	4.1
570	558–575	4.2	2.4	1,354	1,347–1,367	2.7	3.7
587	575–593	0.8	0.5	1,374	1,367–1,378	1.6	2.3
606	593–612	1.6	0.9	1,390	1,378–1,419	4.0	5.6
628	612–632	0.7	0.4	1,435	1,419–1,460	10.6	15.2
642	632–648	0.6	0.4	1,467	1,460–1,472	0.8	1.1
691	648–695	3.5	2.4	1,478	1,472–1,485	1.1	1.7
702	695–718	3.3	2.3	1,495	1,485–1,502	5.1	7.7
725	718–730	2.2	1.6	1,507	1,502–1,513	1.4	2.2
742	730–745	16.2	12.0	1,519	1,513–1,525	2.9	4.5
752	745–756	8.5	6.4	1,537	1,525–1,542	14.2	21.8
767	756–775	5.0	3.8	1,552	1,542–1,557	9.9	15.4
798	775–803	3.2	2.6	1,562	1,557–1,579	2.7	4.2
811	803–820	0.6	0.5	1,590	1,579–1,597	0.9	1.4
854	820–860	2.4	2.0	1,610	1,597–1,634	2.7	4.4
885	860–890	1.7	1.5	1,649	1,634–1,667	0.1	0.1
915	890–930	14.2	12.9	1,686	1,667–1,693	3.4	5.7
946	930–955	1.2	1.1	1,698	1,693–1,705	1.2	2.0
986	955–1018	25.3	24.9	1,710	1,705–1,723	0.2	0.3
Total						426	370

a few critical modes may be required to enhance computational efficiency in such applications.

From the fits, the total Huang-Rhys factors S_{vib} are determined to be 0.72 in 1-propanol and 0.43 in TEA. Similarly, the total emission reorganization energies λ^E are determined to be 650 cm^{-1} and 370 cm^{-1} , respectively; these and other deduced reorganization energies are collected into **Table 3**.

Fluorescence spectra at low resolution can be predicted based on the Δ FLN data analysis by broadening the spectra

from the Huang-Rhys model to match that apparent in experimental low-resolution spectra. Results so obtained are indicated by red dashed lines in **Figure 4**, where they are compared to directly observed low-resolution emission spectra (red solid lines, denoted as EMI). In TEA, the observed and simulated low-resolution spectra are in reasonable agreement, validating the extensive experimental and computational procedures used in obtaining and interpreting the high-resolution Δ FLN data. From low-resolution spectra, the absorption and emission reorganization energies can be

TABLE 3 | Calculated (for methyl Chl-a) and observed (for Chl-a) reorganization energies (in cm^{-1}) for γ -polarized Franck-Condon allowed Q_y absorption (λ^A) and emission (λ^E), compared to analogous results for Pheo-a (Rätsep et al., 2019b) and BChl-a (Rätsep et al., 2011).

Method	Mg Coord.	Pheo-a		BChl-a		Chl-a	
		λ^A	λ^E	λ^A	λ^E	λ^A	λ^E
Obs. ¹ 4.5 K TEA Δ FLN and SEF	-	317	395				
Obs. ¹ low res. 4.5 K TEA	-	355	402				
Obs. ² 1.7 K EtOH/MeOH low res. MCD	-	424					
Obs. ³ 4 K TEA Δ FLN	6				219		
Obs. ^{3,4} 5 K HB	5			378			
Obs. ³ 295 K TEA	5			335	185		
Obs. ³ 4.5 K TEA low res.	6			196	236		
Obs. ³ 4.5 K TEA low res.	-5	-	-	335	260		
Obs. 5 K TEA, low res.	5					$\sim 300^h$	458
Obs. 5 K TEA, Δ FLN	5						370
Obs. 295 K TEA, low res.	5						413
Obs. ² 4 K wet ether FE	5 ^f					262 ^e	
Obs. 295 K wet ether, low res.	5					264 ⁱ	438
Obs. ⁵ 4 K 1-propanol Δ FLN	6						650
Obs. ² 4 K 1-propanol low res.	6					$\sim 420^b$	$\sim 650^a$
Obs. ⁵ 295 K 1-propanol low res.	5					$\sim 490^c$	492
Obs. ^{2,6} PS-I-200 HB	5					547 ^g	
Obs. ^{2,7} WSCP HB	5					645 ^g	
CAM-B3LYP/6-31G* from calc. energies	4	1,214 ^{d,j1}	481 ¹	350 ³	210 ³	607 ²	517 ²
CAM-B3LYP/6-31G* from scaled frequencies	4			300 ³	200 ³	567	492
B3LYP/6-31G* from calc. energies	4	184 ¹	165 ¹	130 ³	150 ³	243	245
MN15/6-31G* from calc. energies	4	493 ¹	282 ¹	184	167	390	358
ω B97XD/6-31G* from calc. energies	4	1,609 ^{d,j1}	594 ¹	310 ³	1,140 ³	713	606

^aObserved spectrum (Rätsep et al., 2009a) is deconvoluted (see **Figure 5**) into two bands representing the dominant 6-coordinate species (85%) and a secondary 5-coordinate one using the spectral bandshape from Δ FLN, indicating that the Δ FLN results accurately depict traditional low-resolution data.

^bObserved absorption and MCD spectra are fitted to a model depicting 85% 6-coordinate species, scaling the bandshape observed in wet ether by FE (see **Figure 6**) (Reimers et al., 2013).

^cVery crude estimate for the 5-coordinate species assuming that the x polarized absorption commences is located 1,000 cm^{-1} above Q_x origin and has the same intensity as that observed for the 6-coordinate species.

^dOne poorly represented mode depicting aromaticity in Q_y involving interactions with nitrogen lone-pair orbitals; neglecting this results become CAM-B3LYP 465 cm^{-1} , ω B97XD 475 cm^{-1} .

^eAfter removal of Q_x using full-quantum spectral simulations (Reimers et al., 2013).

^fLigand is water (Reimers et al., 2014).

^gFrom hole-burning (HB) data, but qualitatively unreliable owing to baseline uncertainties (Reimers et al., 2013).

^hAfter approximate removal of Q_x band using the bandshape deduced in wet ether (Reimers et al., 2013).

ⁱFrom analytical inversion (Reimers and Krausz, 2014) of absorption and MCD data (Umetsu et al., 1999).

^jReferences: 1- (Rätsep et al., 2019b), 2- (Reimers et al., 2013), 3- (Rätsep et al., 2011), 4- (Zazubovich et al., 2001), 5- (Rätsep et al., 2009a), 6- (Gillie et al., 1989), 7- (Hughes et al., 2010).

determined using

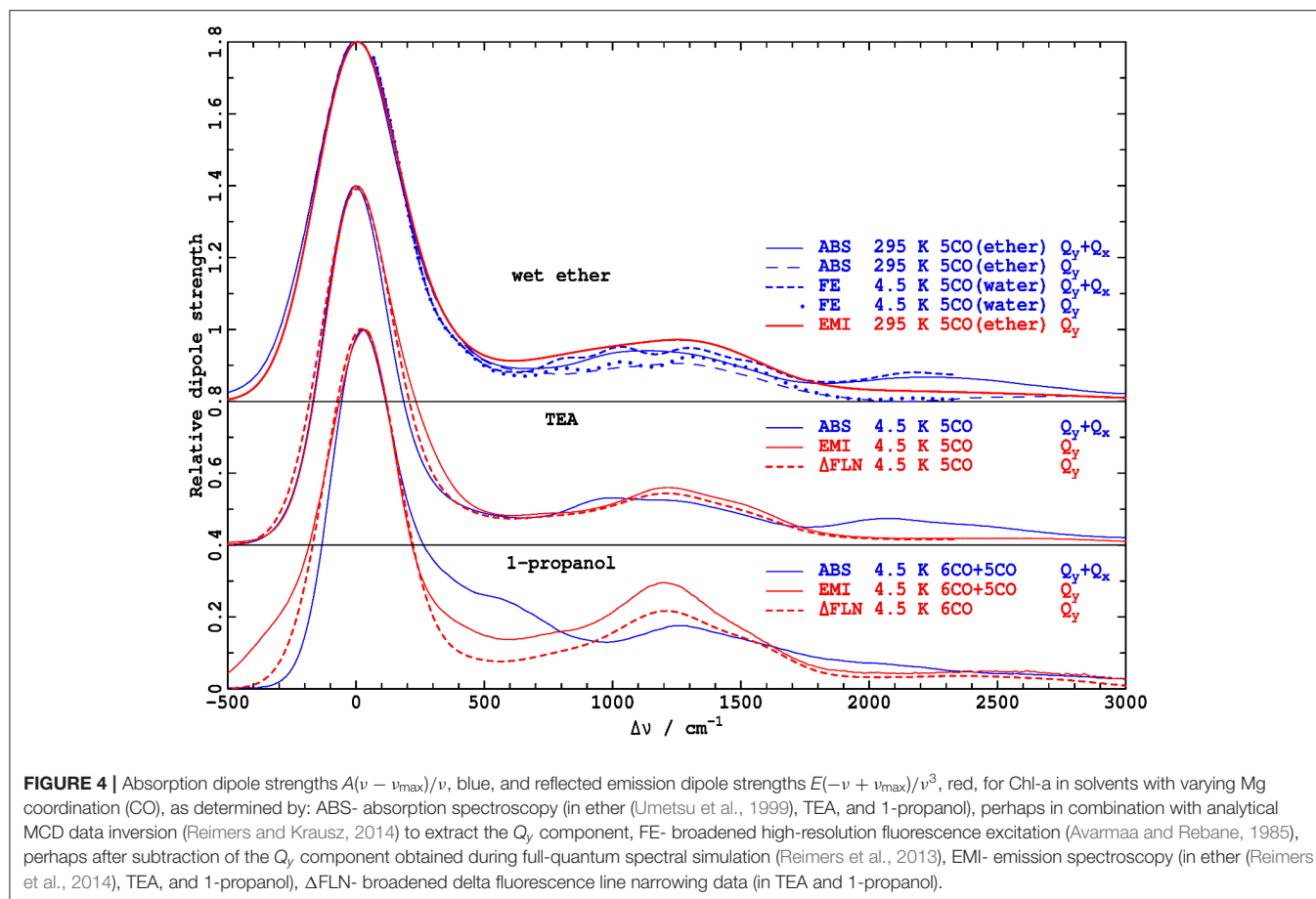
$$\lambda^A = h \frac{\int_0^\infty A(\nu) d\nu}{\int_0^\infty A(\nu)/\nu d\nu} - h\nu_{00},$$

$$\lambda^E = h\nu_{00} - h \frac{\int_0^\infty E(\nu)/\nu^2 d\nu}{\int_0^\infty E(\nu)/\nu^3 d\nu}, \quad (9)$$

respectively, where $A(\nu)$ is the observed absorption coefficient and $E(\nu)$ the observed emission intensity. Note that, as emission intensities are sensitive to the spectral scan rate, $E(\nu)$ corresponds to the emission observed when the spectrum is scanned at a constant rate of change of frequency; spectra $E(\lambda)$ scanned at a constant rate of change of wavelength $\lambda = c/\nu$ are related via $E(\nu) = E(\lambda)/\nu^2$. For TEA,

taking ν_{00} to be the frequency of the broad ZPL maximum, this gives $\lambda^E = 458 \text{ cm}^{-1}$, larger than the Δ FLN value of 370 cm^{-1} .

Much larger differences are seen in **Figure 4** for the analogous comparison of low-resolution spectra obtained by broadening the Δ FLN spectrum and from direct observation of emission in 1-propanol. A plausible explanation of the difference is that some Chl-a molecules have 5-coordinate Mg atoms, even at the low temperatures used; the Δ FLN spectra select only for the major (6-coordinate) component, whereas the EMI spectrum captures all emission. In **Figure 5**, the observed low-resolution emission spectrum is approximately separated into 5-coordinate (15%) and 6-coordinate (85%) components, yielding a 6-coordinate reorganization energy of $\sim 650 \text{ cm}^{-1}$, in good agreement with the value obtained for the pure 6-coordinate species using Δ FLN.



Analogous data pertaining to the Q_y absorption spectrum of Chl-a is difficult to obtain owing to interference from the Q_x band. High-resolution fluorescence excitation (FE) spectra of Chl-a have been measured by Avarmaa and Rebane (1985), and subsequently the doubly-peaked x -polarized intensity was subtracted using an extensive quantum-mechanical non-adiabatic coupling model, combined with a Huang-Rhys analysis of the observed vibrational structure (Reimers et al., 2013). The resulting Q_y vibrational frequencies and Huang-Rhys factors are reproduced in **Supplementary Table 6**. The solvent used by Avarmaa and Rebane is best characterized as wet ether (Reimers et al., 2014), with, at the low temperatures used, water coordinating the chlorophyll Mg atom. The original observed FE spectrum, as well as that after subtraction of Q_x , both after broadening to match low-resolution (Umetsu et al., 1999) absorption spectra observed in ether at room temperature, are shown in **Figure 4**. In an alternate approach, the Q_x component of the room-temperature absorption (ABS) spectrum has been subtracted using an analytical technique for the inversion of observed absorption and magnetic circular dichroism (MCD) data (Reimers and Krausz, 2014). The total absorption and resulting Q_y -component spectrum are also shown in the figure.

As seen, the full absorption spectrum is in good agreement with that obtained by broadening the observed FE spectrum, and the two Q_y -only components are also in good agreement. Both approaches lead to the conclusion that the absorption

reorganization energy is $\lambda^A = 262 \text{ cm}^{-1}$, much less than the emission reorganization energy determined from the low-resolution room-temperature spectrum in ether, $\lambda^E = 438 \text{ cm}^{-1}$. This is visually very apparent from the absorption and fluorescence spectra compared in **Figure 4**.

Similar accurate descriptions of the Q_y absorption in 1-propanol and TEA are not available. Yet rough estimates can be made by partitioning x and y polarization, assuming that the Q_x band profile is not solvent dependent, and, for 1-propanol, as in **Figure 5**, that the Q_y absorption bandshape of the 5-coordinate species is the same as that for the 6-coordinate one. Results for the separation of the two species in 1-propanol at 4 K are shown in **Figure 6**. They provide rough estimates of absorption reorganization energy of $\lambda^A = 420 \text{ cm}^{-1}$ for the 6-coordinate species and 490 cm^{-1} for the 5-coordinate one. As for ether, absorption reorganization energies appear to be much less than those in emission.

Relating the Observed High-Resolution Absorption and Emission Properties Based Upon DFT Calculations of the Duschinsky Matrix

From **Figure 3**, as well as **Tables 1, 2**, and **S6**, it is clear that the vibrational frequencies in different solvents and in the S_0 ground state and Q_y excited states are quite similar, yet the vibrational

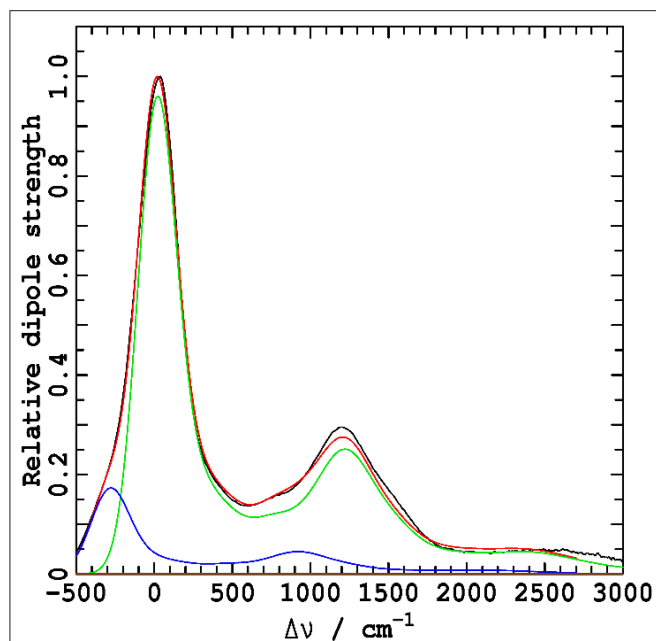


FIGURE 5 | The observed emission spectrum of Chl-a in 1-propanol at 4.5 K (black, the EMI spectrum from **Figure 4**) is interpreted in terms of contributions from molecules with 6-coordinate Mg (green, 85%) and 5-coordinate Mg (blue, 15%). The 6-coordinate component bandshape is taken to be that as observed by Δ FLN, broadened with a Gaussian inhomogeneous distribution function fitted with $\text{FWHM} = 280 \text{ cm}^{-1}$ (taken from **Figure 4**). The 5-coordinate component bandshape is crudely taken to be the same as that for the 6-coordinate species. In this way, the fit is done using only three adjustable parameters: the relative component composition, the component ZPL frequency difference, and the FWHM. The sum of the two contributions is shown in red and closely approximates the observed emission.

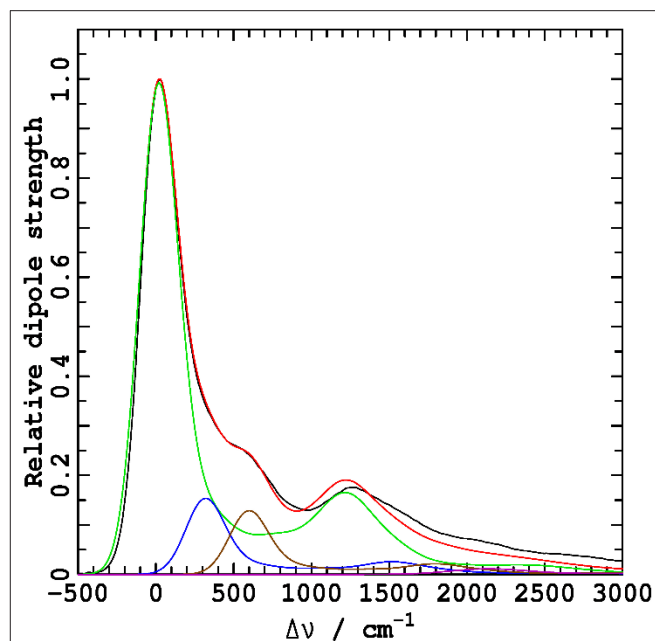


FIGURE 6 | Separation of the observed (Rätsep et al., 2009a) absorption spectrum $A(\nu)$ of Chl-a in 1-propanol at 4.5 K, frequency-weighted as $A(\nu)/\nu$ to reveal the dipole strength (black), into two y-polarized components arising from molecules with 6-coordinate magnesium (green, 85%) and 5-coordinate magnesium (blue, 15%, 295 cm^{-1} higher in energy), and the x-polarized intensity (blue, the result of strong non-adiabatic coupling between vibrational lines of Q_y and the Q_x origin), using for it the spectral profile extracted from MCD data in wet ether (Reimers et al., 2013). The two absorption bandshape profiles are assumed to be the same and are set to that depicted by the bandshape for Chl-a in wet ether at 4.2 K determined from FE (**Supplementary Table 3**), located and scaled to fit the observed absorption (red).

intensities (Huang-Rhys factors) and associated reorganization energies can show large differences. Vibrational motions in the two states are clearly similar, but small differences can have profound effects. For example, two (or more) modes of very similar frequencies can mix strongly with each other as a function of small environmentally introduced changes in their frequency differences, moving in and out of resonance. Alternatively, one mode can retain its basic form in the other state yet mix very slightly with a large number of modes that span a wide frequency range. While the mixing with any one mode remains small, the effects of mixing with many modes can reinforce each other to manifest profound consequences. To quantify this, the required tool is the Duschinsky rotation matrix

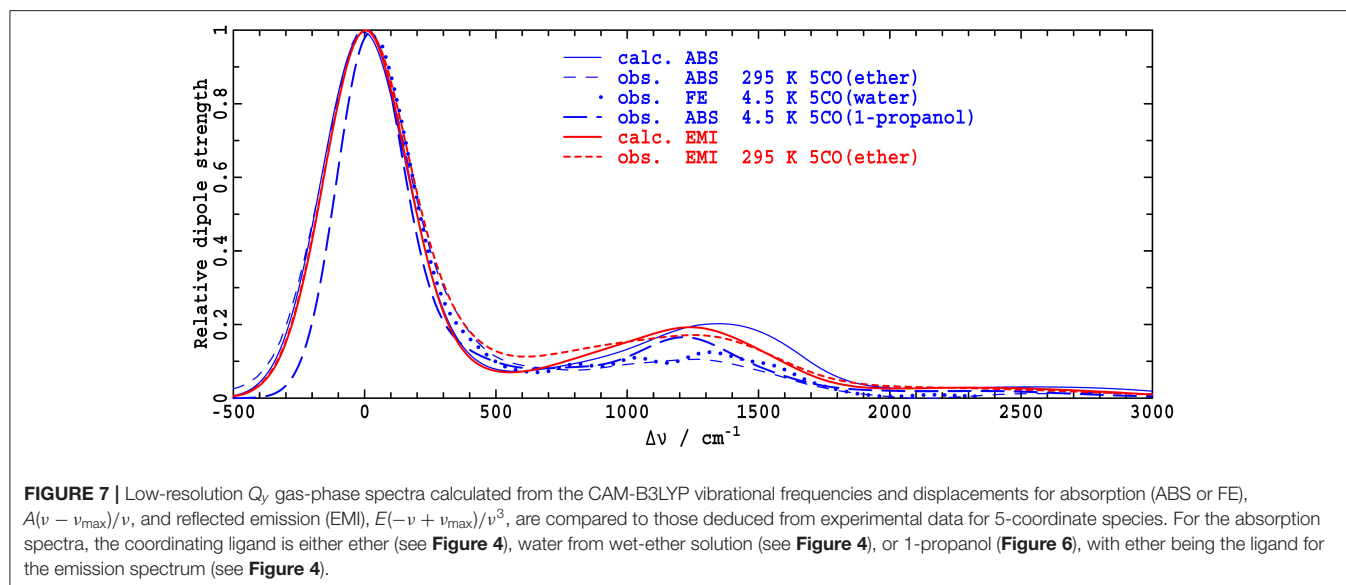
$$\mathbf{D} = (\mathbf{C}^{S_0})^T \mathbf{C}^{Q_y} \quad (10)$$

where \mathbf{C}^{S_0} are the normal modes of vibration of the ground state and \mathbf{C}^{Q_y} are those for the excited state. These normal-mode matrices are expressed in terms of mass-weighted Cartesian coordinates. Duschinsky matrices can also be used to understand how the normal modes of vibration respond to other changes, e.g., solvent changes. Unfortunately, the Duschinsky matrix contains n^2 elements, where n is the number of

vibrational modes, for which little direct evidence is provided by experimental measurements, as most observed properties depend on combinations of multiple Duschinsky-matrix elements.

Following the success with similar studies on BChl-a (Rätsep et al., 2011) and Pheo-a (Rätsep et al., 2019b), we turn to DFT calculations of \mathbf{D} to relate the vibrational motions of the S_0 and Q_y states of Chl-a. To be useful, such calculations must first describe adequately the Huang-Rhys factors pertinent to absorption and emission. Unfortunately, previous experience with chlorophyllide spectral modeling has indicated that different possible density-functional approaches, as well as alternative *ab initio* or semi-empirical methods, can lead to errors in predicted reorganization energies by an order of magnitude or much more, as well as predicted absorption and/or emission profiles that do not resemble those observed (Rätsep et al., 2011, 2019b). To find a suitable computational method, we sampled four DFT approaches—CAM-B3LYP (Yanai et al., 2004; Kobayashi and Amos, 2006), B3LYP (Becke, 1993), MN15 (Yu et al., 2016), and ω B97XD (Chai and Head-Gordon, 2008)—as these have previously offered results of interest.

The observed and calculated emission and absorption reorganization energies for Chl-a are compared in **Table 3**, along



with those for Pheo-a and BChl-a. CAM-B3LYP was previously identified (Rätsep et al., 2011, 2019b) as the best choice for BChl-a and Pheo-a, and this remains the case for Chl-a too. It is a hybrid functional with asymptotic potential correction, a type of method identified as the entry level for spectroscopic calculations on aromatic molecules (Cai et al., 2006) (as is ω B97xD, but ω B97xD is prone to larger errors). Using B3LYP, low chlorophyllide reorganization energies similar to the experiment have been predicted, but the associated spectral profiles have had no relationship to those observed. MN15 appears to be a method of interest and the only identified alternative to CAM-B3LYP. Yet CAM-B3LYP and MN15 both showed serious failures for a single, though different, mode in absorption for Pheo-a (Rätsep et al., 2019b). Hence, we see that just because a method usefully describes most vibrations of interest, it does not mean that all such vibrations are reliably defined. For CAM-B3LYP, the poorly described mode depicts aromaticity in the Q_y state and is affected by non-adiabatic coupling to nitrogen (n, π^*) states that only exist in pheophytins, so the error is not relevant to Chl-a.

That the CAM-B3LYP results present a useful starting point for understanding the observed high-resolution data that is demonstrated in **Figure 7**, where low-resolution simulated absorption and emission spectra are compared to observed results. The calculated gas-phase emission spectrum closely resembles the shown observed emission in ether at 295 K, with the differences being less than the observed changes presented in **Figure 4** as a function of solvent. The calculated gas-phase absorption spectrum depicts a 0–1 vibrational sideband in the 800–1,600 cm^{-1} region that is significantly enhanced compared to the shown observed spectra taken in ether, and somewhat enhanced compared to the observed spectrum (taken from **Figure 6**) in 1-propanol. Such enhancements are expected based on the overestimation of the absorption reorganization energy reported in **Table 3**. Of note, however, is that this effect is not mode specific and

hence a qualitatively indicative depiction of the high-resolution information is expected.

The computational method chosen must also accurately represent the vibrational frequencies of Chl-a. In applying CAM-B3LYP results to interpret chlorophyllide spectra, it is common to rescale the force constants as a crude correction for anharmonicity (Rätsep et al., 2011, 2019b), which slightly reduces the calculated reorganization energies, to make them closer to those observed (**Table 3**). Analogously scaled CAM-B3LYP/6-31G* values are known to reproduce the observed high-resolution data for 90 vibrations of porphyrin to within a root-mean-square error of 22 cm^{-1} (Rätsep et al., 2019b), and hence are expected to be reliable also for Chl-a.

Table 4 presents the high-resolution results from the CAM-B3LYP calculations in terms of modes of Q_y , predicted to dominate absorption, modes of the ground state predicted to dominate emission, and the critical Duschinsky matrix elements that interconnect them. Some key modes in one state may be directly mapped onto key modes in the other state, the simple situation that gives rise to absorption-emission asymmetry, but other key modes are extremely mixed and have no clear assignment, leading to the absence of absorption-emission asymmetry. In the table, 30 of the 37 observed modes listed for absorption and/or emission are assigned to calculated modes based on proximity and reorganization energy. This mapping includes the most important modes either observed or calculated in both absorption and emission. It is thus likely that the analysis captures the essential qualitative elements of the intrinsic relationships, without addressing important quantitative subtleties such as the observed dependence of emission on solvent and coordination. Indeed, most observed modes in emission are related to those in absorption by this procedure.

How the Duschinsky matrix elements control absorption/emission asymmetry is shown in **Figure 8**. In

TABLE 4 | Tentative relationships between observed Chl-a Q_y vibrational modes (Reimers et al., 2013) from fluorescence excitation (Avarmaa and Rebane, 1985) in wet (Reimers et al., 2014) ether at 4.2 K and observed S_0 modes from FLN in 1-propanol or TEA at 4.5 K, see **Tables 1, 2**.

1Q_y FE wet ether		1Q_y calc.		1Q_y assignment in terms of S_0 modes		S_0 calc.		S_0 Δ FLN TEA		S_0 Δ FLN 1-propanol	
ν_i	λ_i	ν_i	λ_i			ν_i	λ_i	ν_i	λ_i	ν_i	λ_i
-	-							22	0.3	-	-
		64	16	42% 64, 28% 41, 19% 54		41, 64	12				
110	1	96,99	7	100% 93, 89% 99		93,99	7	99	2	92 ^b	4 ^b
190	1	155	5	98% 154		154	5	170–210	1	194	3
263	2	241,263	3	96% 244, 95% 267		244,267	3	263	4	267	9
344	3	343	4	98% 345		345	2	349	6	353	11
370–390	3	375,385	4	95% 388, 82% 391		388,391	3	370–390	5	370–390	7
435–470	1	464	2	75% 470		470	2	430–450	1	430–450	5
		494	2	81% 501		501	3				
515	0.3	505	3	75% 513		513	1	520	4	519	7
563	3	589	2	99% 593		593	2	570	2	573	7
739	11	731,735	20	60% 737, 51% 749, 35% 739		737,739	16	742	12	745	36
788	3	837	4	87% 839		839	2	798	3	798	9
925	3	917	7	39% 895, 24% 897		895,897	15	915	13	914	25
966	23	977,979	36	87% 977, 45% 986		977	40	986	25	985	31
1,034	6							1,046	7	1,043	25 ^c
1,070	8	1,084, 1,092	8	91% 1093		1,093	1	1,071	5	1,064	18 ^c
1,107	4	1,110	2	50% 1,110, 17% 1,102, 18% 1,122		1,102, 1,122	3	1,109	5	1,107	13 ^c
1,132	5	1,131	15	70% 1,131, 18% 1,149		1,131	10	1,117	5	1,120	18
						1,149 ^a	12	1,144	18	1,146	42
1,165	8	1,159	14	37% 1167		1,167	12	1,183	18	1,183	55
1,196	5	1,193	9	38% 1,184, 5% 1,192		1,192	5	1,209	17		
		1,212	5	33% 1,221, 60% 1,211		1,211	26	1,236	9		
1,228	15	1,224	47	23% 1,211, 60% 1,221		1,221	35	1,223	17	1,224	69
1,253	18	1,260	15	89% 1262		1,262	11	1,263	8	1,261	10
1,286	16	1,285, 1,287, 1,288	13	86% 1,283, 82% 1,286, 60% 1,287		1,286, 1,287, 1,288	9	1,288	7	1,288	18
		1,306	6	26% 1,288, 16% 1,312, 17% 1348		1,288 ^a	3				
		1,323	10	46% 1324, 20% 1338, 11% 1331		1,324	17	1,306	4	1,306	24
		1,329	12	31% 1,321, 27% 11,348, 15% 1,338		1,321 ^a	37	1,329	23	1,324	39
1,332	18	1,332	17	56% 1,331, 16% 1,321, 11% 1,338		1,331	0				
						1,338 ^a	4	1,354	4	1,352	12
1,369	10	1,364	4	44% 1,366, 12% 1,380, 13% 1,388		1,366	2	1,374	2	1,374	10
1,393	7	1,392	7	22% 1,396, 17% 1,380, 14% 1,384		1,396	5	1,390	6	1,388	12
1,415	6	1,423	10	31% 1,458, 18% 1,441							
		1,424	5	48% 1,422, 25% 1,441		1,422	5				
						1,441	5	1,435	15	1,436	23
		1,459	0	57% 1,465		1,458	5	1,467	1	1,488	6
1,446	8	1,466	3	45% 1,470, 13% 1,522		1,470	0				
1,510 ^d	18	1,501	15	55% 1,481, 1,486		1,481, 1,486	24	1,519	5	1,517	18
1,530	9	1,530	66	46% 1,538, 24% 1,590		1,538	26	1,537	22	1,531	18
1,587	11	1,570	42	24% 1,562, 17% 1,568		1,568	11	1,552	15	1,552	17
		1,595	29	54% 1,617, 19% 1,590		1,617	8	1,686	6	1,654	10
1,665	4	1,608	3	45% 1,590, 24% 1,617		1,590	11	1,610	4	1,596	2
	188			415 Total, listed modes			355		301		500
	262			567 Total, all modes			492		370		650

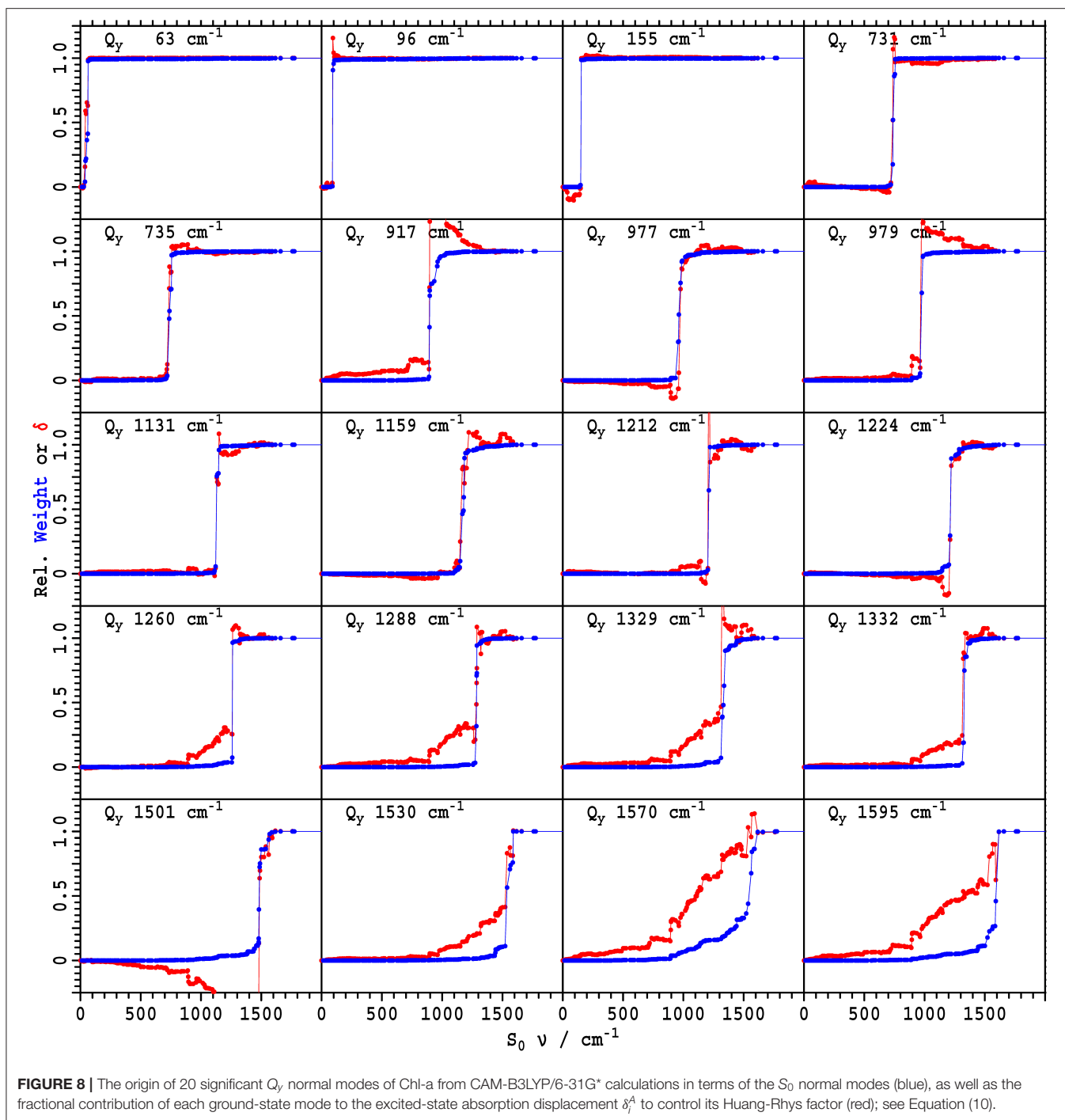
These are obtained by assigning the observed lines to modes calculated for methyl Chl-a using CAM-B3LYP and the calculated Duschinsky matrix elements to map the calculated modes of Q_y onto those of S_0 .

^aNo clear assignment, distributed over many Q_y modes.

^bIt is unclear as to whether all or part of this emission should be attributed to intramolecular vibrations, as reported in this table and elsewhere, or else to intermolecular phonons; modes of lower frequency are not easily identifiable in spectra.

^cNo plausible assignment.

^dBroad band, originally listed at 1,493 cm^{-1} but the peak in this region is at 1,510 cm^{-1} .



this figure, for 20 vibrational modes of Q_y , the mode origin and the development of its Huang-Rhys factor is indicated in terms of contributions from each ground-state mode. The Huang-Rhys factors in absorption and emission, S_i^A and S_i^E , respectively, can be expressed as

$$S_i^A = (\delta_i^A)^2 / 2 \text{ and } S_i^E = (\delta_i^E)^2 / 2 \quad (11)$$

in terms of dimensionless nuclear displacements on the ground state δ_i^E and excited state δ_i^A

$$\delta_i^E = - \left(\frac{2\pi \nu_i^{S_0}}{\hbar} \right)^{1/2} \sum_{j=1}^N C_{ji}^{S_0} m_j^{1/2} \Delta x_j, \\ \delta_i^A = \left(\frac{2\pi \nu_i^{Q_y}}{\hbar} \right)^{1/2} \sum_{j=1}^N C_{ji}^{Q_y} m_j^{1/2} \Delta x_j, \quad (12)$$

where Δx_j is the change in Q_y from S_0 of a Cartesian coordinate of an atom of mass m_j , or its equivalent after curvilinear transformation (Reimers, 2001). The displacements are related through the Duschinsky matrix (Equation 10) as

$$\delta_i^A = - \sum_{k=1}^n \left(\frac{v_i^{Q_y}}{v_k^{S_0}} \right)^{1/2} D_{ki} \delta_k^E, \text{ where } 1 = \sum_{k=1}^n D_{ki}^2 \quad (13)$$

(Note that the Duschinsky matrix is orthogonal in rectilinear coordinates but not necessarily so in curvilinear coordinates, see **Supplementary Material** for the details of treatment in this case). Of interest, the frequency-weighting term in Equation (13) shows how low-frequency modes in emission can preferentially contribute to absorption intensity.

Full depictions of how each ground-state mode contributes to the vibrational density and displacement (Equation 13) are provided in **Supplementary Figures 1, 2**. For some key modes, enhanced descriptions are provided in **Figure 8**. This figure shows the cumulative contribution D_{ik}^2 of each ground-state vibration k to the excited state vibration i , which is shown in blue (also some key contributions are listed in **Table 4**). Typically, just a small number of ground-state modes mix to form each excited state, with the blue curves approximating Heaviside step functions. Hence a close correlation is observed between ground- and excited-state vibrational frequencies, with the resulting frequencies depending only on sums of densities D_{ik}^2 . Shown also in red are the (fractional) cumulative contributions $\left(v_i^{Q_y} / v_k^{S_0} \right)^{1/2} D_{ik} \delta_k^E / \delta_i^A$ of each ground-state mode to the excited-state displacement δ_i^A . As these contributions to the displacement are signed, the Huang-Rhys factors embody both constructive and destructive interferences. When the shown curves resemble Heaviside step functions, there is symmetry between absorption and emission (i.e., the transition moment in absorption matches that in emission), but in many cases interferences dominate and absorption/emission symmetry is lost.

A simple case (**Figure 8, Table 4**) is the mode predicted in absorption at 155 cm^{-1} and in emission at 154 cm^{-1} , with a similarity of 98% as revealed by the Duschinsky matrix. These vibrations are attributed to the significant absorption and emission observed in the 190 cm^{-1} region.

Next, we consider some lines with large reorganization energy observed in Q_y at $1,228 \text{ cm}^{-1}$ with $\lambda^A = 47 \text{ cm}^{-1}$ that is assigned to ground-state modes observed at $1,223 \text{ cm}^{-1}$ with $\lambda^E = 17 \text{ cm}^{-1}$ in TEA and at $1,224 \text{ cm}^{-1}$ with $\lambda^E = 69 \text{ cm}^{-1}$ in 1-propanol. The calculations indicate that two modes (23% $1,211 \text{ cm}^{-1}$ and 60% $1,221 \text{ cm}^{-1}$) mix to dominate the observed effects, sometimes constructively and sometimes destructively. Such mixing could explain the observed very large solvent dependence of the ΔFLN spectra, as it would be very sensitive to the environment. This mode has the largest observed reorganization energy in the ΔFLN spectra in 1-propanol, but a similar situation is found also for the 2nd-largest mode observed at $1,183 \text{ cm}^{-1}$ in both 1-propanol and TEA, this time presenting solvent-dependent reorganization energies of 55 cm^{-1} and 18 cm^{-1} , respectively. For the 2nd-largest mode, the calculations indicate that various ground-state modes contribute to the

excited-state vibration (calculated at $1,159 \text{ cm}^{-1}$), again allowing solvent effects to dramatically change mode intensities. A similar situation exists for the mode with the largest reorganization energy observed by ΔFLN in TEA (at 986 cm^{-1}) that is assigned to interference between the calculated ground-state vibrations at 977 cm^{-1} and 979 cm^{-1} .

Also of interest are the modes with large reorganization energy observed by ΔFLN in TEA at $1,144 \text{ cm}^{-1}$ and in 1-propanol at $1,146 \text{ cm}^{-1}$. These are assigned to a calculated ground-state vibration at $1,149 \text{ cm}^{-1}$ that is made up of many small contributions from excited-state modes spanning $1,100$ – $1,300 \text{ cm}^{-1}$. Hence the calculations predict that this intense mode in emission has no counterpart in absorption, and indeed no counterpart is obvious from the observed fluorescence-excitation spectra.

Lastly, we consider eight example modes from the important high-frequency region calculated in Q_y between $1,260$ and $1,595 \text{ cm}^{-1}$ (**Figure 8, Table 4**). For these, the absorption Huang-Rhys factor is predicted to arise following extensive constructive interference involving many ground-state modes ranging often over $1,000 \text{ cm}^{-1}$ in frequency. Emission/absorption symmetry is intrinsically lost through this process. The larger the number of modes involved and the greater the spread of frequencies, the more similar the reorganization energies observed by ΔFLN in TEA and in 1-propanol become. Hence, for the high-frequency modes, the major effect of solvent variation becomes frequency shifts associated with localized aspects of solvation. Also, energy absorbed by one of these high-frequency modes, in the absence of relaxation processes, will be re-emitted by all coupled ground-state modes and hence can be spread out into a band that is over $1,000 \text{ cm}^{-1}$ wide.

In **Supplementary Material**, analogous results to those in **Table 4** are presented in **Supplementary Table 2** for the situation in which one 1-propanol ligand is bound to the Mg of Chl-a. Unfortunately, as detailed in **Supplementary Table 1**, approaches such as this using explicit solvation and/or implicit solvation fail to reproduce the basic observed changes in the absorption and emission reorganization energies from **Table 3**. Hence, details in the differences found between the high-resolution analyses presented in **Table 4, Supplementary Table 2** are not expected to be meaningful. There are two qualitative features of interest, however. First, the basic pattern depicted in **Table 4** does not change, indicating that many key calculated features are invariant to the treatment of solvation. Second, the calculations predict that some bands undergo small frequency changes but factors of three change in intensity, in going from the isolated molecule to the 1-propanol cluster, just as observed modes show large changes in intensity on changing the solvent from TEA to 1-propanol (**Supplementary Table 3**). Therefore, in principle, the calculations embody all features needed to interpret the experimental data.

CONCLUSIONS

The experimental data fitting is done adopting a Huang-Rhys model (Huang et al., 1950). This assumes that just two

electronic states are involved, that the Born-Oppenheimer (Born and Oppenheimer, 1927) and Franck-Condon (Condon, 1928) approximations hold, that the potentials-energy surfaces are harmonic, that the ground- and excited-state vibrational frequencies are identical, and that the Duschinsky rotation matrix (Duschinsky, 1937) is the unit matrix, yielding vibrational frequencies ν_i , Huang-Rhys factors S_i , and associated reorganization energies $h\nu_i S_i$ for each state. Unfortunately, this analysis is lacking in that it allows different vibrational frequencies to be determined for each state yet is internally based on the assumption that the same vibrational frequencies occur in each state. To resolve this paradox, the experimental data is augmented with the Duschinsky rotation matrices from the DFT calculations, providing links between the observed modes in absorption and those in emission. The simulated spectra therefore correspond to a modified Huang-Rhys model, in which the initial-state vibrational frequency is taken to be the average initial-state frequency, as weighted by the Duschinsky-matrix elements pertaining to each excited-state frequency (Reimers, 2001). A feature of the calculations, which is sometimes critical and sometimes not, is the use of a harmonic potential approximation in curvilinear coordinates to take into account the often very large anharmonic effects operative in large molecules (Reimers, 2001). The net result is that each intense high-resolution line in absorption is mapped onto an absorption mode predicted by the calculations. This mapping is accomplished by: (1) assigning a key observed line in absorption to lines predicted in the calculations, (2) applying the calculated Duschinsky matrix to the predicted line onto one or more lines calculated in emission, and (3) assigning the predicted emission line(s) onto an observed emission line(s). This allows the observed high-resolution absorption-emission asymmetry to be understood.

Theoretical prediction of absorption and emission spectra, for a molecule the size of chlorophyll, to the accuracy needed to interpret either low-resolution or high-resolution spectra, remains a serious challenge. Required is the determination of the optimized geometry, vibrational frequencies, and associated normal modes of vibration in both the ground and excited electronic states. The only readily applicable approach of reasonable accuracy is DFT, applied using its time-dependent formalism (Casida, 1995) (TD-DFT) to model excited states. One needs to choose between a wide variety of available density functionals, however, with a desired outcome being that any sensible choice leads to the same basic qualitative conclusions. Also, previous similar studies for BChl-a and Pheo-a indicate that different modern approaches can predict results showing great disparity, with most not even qualitatively depicting the basic observed absorption and emission spectral properties (Rätsep et al., 2011, 2019b). A reason for this is that a critical property responsible for the usefulness of the chlorophyllides in light harvesting, transport, and energy conversion is the very low value of their emission and absorption reorganization energies, resulting in difficult quantitative calculations that portray related properties. The only satisfactory density functional so far identified is CAM-B3LYP (Yanai et al., 2004; Kobayashi and

Amos, 2006); the conclusion confirmed also here in case of Chl-a. This is a functional embodying long-range correction of the potential so as to be able to treat charge-transfer states, without which the lowest-energy non-charge transfer states like Q_y and Q_x are poorly represented (Cai et al., 2002, 2006; Magyar and Tretiak, 2007; Peach et al., 2008).

While the highly environment sensitive contribution of the Q_x state to absorption has long been known as a major source of asymmetry between observed low-resolution absorption and emission spectra of Chl-a, the measurement before (Rätsep et al., 2009a) and herein of phonon-sideband-free high resolution emission spectra using Δ FLN, to complement existing high-resolution absorption spectra (Avarmaa and Rebane, 1985), indicates that significant asymmetry remains even after the effects (Reimers et al., 2013) of Q_x absorption are negated. Further, measuring Δ FLN in two different solvents, TEA which results in 5-coordinate magnesium, and 1-propanol, with the coordination increasing to 6, reveals strong solvent-dependence for vibrational line intensities. With the exception of vibrational modes involved in specific solvation effects, only small changes in vibrational frequency are found to accompany these large changes in line intensity. Also, as found for BChl-a (Rätsep et al., 2011) and Pheo-a (Rätsep et al., 2019b), the most intense vibrational lines observed in either one of absorption or emission can be absent in the other spectroscopic results, indicating that absorption-emission asymmetry arises from fundamental changes in the vibrational descriptions of the S_0 and Q_y states.

The large absorption-emission asymmetry, as well as the strong solvent dependence of the emission line strengths, is attributed to properties of the Duschinsky rotation matrix that maps the form of the vibrational motions in Q_y onto those of S_0 . Four distinct types of properties are predicted and correlated with experimental observations: (1) some modes retain their form in the two electronic states, leading to high-resolution absorption/emission symmetry; (2) some modes mix strongly with just a few other modes of similar frequency, making line intensities strongly dependent on subtle solvent-induced changes in frequency of the coupled modes, as well as providing significant absorption/emission asymmetry; (3) some modes mix very strongly, so strong that dominant lines in either absorption or emission have no counterpart; and (4) strong mixing, particularly for key high-frequency modes, can result in absorption at one vibrational frequency, without phase loss or energy relaxation, producing emission spanning over a thousand cm^{-1} .

These results are particularly pertinent to computational modes describing exciton transport in photosystems. If vibrational relaxation occurs before reemission, then quantum coherence of the energy-transport process is lost, reducing the process to one of classical kinetics, with re-emission expected over the broad allowed range. If there is no vibrational relaxation and full absorption-emission asymmetry, then energy is simply stored on a chromophore and then passed on coherently. The modeling of exciton transport usually involves understanding the competition between these processes, competition between

coherent and incoherent transport mechanisms. A new dimension to this is demanded by the results obtained: a chromophore that absorbs an exciton at a specific energy can also coherently reemit it, in a very mode-specific way, over a wide energy range. Energy change and decoherence are therefore no longer intrinsically coupled.

Finally, we note that the calculations embody all effects needed for a detailed understanding of the effects of solvent on high-resolution spectroscopic properties, but still fail to qualitatively describe the actual observed effects. It is likely that large-sample modern treatments that fully solvate the chromophore with explicitly represented solvent molecules, combined with inclusion of long-range dielectric properties (Hush and Reimers, 2000; Skyner et al., 2015; Zuehlsdorff and Isborn, 2018; Cerezo et al., 2020), are required for further progress.

DATA AVAILABILITY STATEMENT

The original contributions presented in the study are included in the article/Supplementary Material, further inquiries can be directed to the corresponding author.

AUTHOR CONTRIBUTIONS

JR designed and performed the calculations and spectral data fitting. MR performed the sample preparation and experimental

measurements. AF designed the research. All authors contributed to the manuscript.

FUNDING

We thanked the Estonian Research Council (grant PRG664) for support of the experimental work and the National Computational Infrastructure (NCI), INTERSECT, the Chinese National Natural Science Foundation (grant #11674212), and the Shanghai University ICQMS computational facility for support of the computational work.

SUPPLEMENTARY MATERIAL

The Supplementary Material for this article can be found online at: <https://www.frontiersin.org/articles/10.3389/fchem.2020.588289/full#supplementary-material>

Supplementary Material provided for (i) additional results tables, (ii) data files providing the optimized coordinates \mathbf{x} , vibrational frequencies \mathbf{v} , and normal modes \mathbf{C} of methyl Chl-a porphyrin in its ground state Q_y state, as well as the associated Duschinsky matrix \mathbf{D} and curvilinear projections δ^A and δ^E of the ground-to-excited state geometry changes onto the two sets of normal modes, and the associated reorganization energies, and (iii) pdf files showing pictorially the form of the ground-state and excited-state normal modes.

REFERENCES

- Adolphs, J., Berrner, M., and Renger, T. (2016). Hole-burning spectroscopy on excitonically coupled pigments in proteins: theory meets experiment. *J. Am. Chem. Soc.* 138, 2993–3001. doi: 10.1021/jacs.5b08246
- Avarmaa, R. A., and Rebane, K. K. (1985). High-resolution optical spectra of chlorophyll molecules. *Spectrochim. Acta A* 41, 1365–1380. doi: 10.1016/0584-8539(85)80189-6
- Becke, A. D. (1993). Density-functional thermochemistry. III. The role of exact exchange. *J. Chem. Phys.* 98, 5648–5652. doi: 10.1063/1.464913
- Blankenship, R. E., Madigan, M. T., and Bauer, C. E. (eds.). (2004). *Anoxygenic Photosynthetic Bacteria*. Dordrecht: Kluwer.
- Born, M., and Oppenheimer, R. (1927). Zur Quantentheorie der Molekeln (On the quantum theory of molecules). *Ann. Phys.* 389, 457–484. doi: 10.1002/andp.19273892002
- Bukarte, E., Haufe, A., Paleček, D., Büchel, C., and Zigmantas, D. (2020). Revealing vibronic coupling in chlorophyll c1 by polarization-controlled 2D electronic spectroscopy. *Chem. Phys.* 530:110643. doi: 10.1016/j.chemphys.2019.110643
- Cai, Z.-L., Crossley, M. J., Reimers, J. R., Kobayashi, R., and Amos, R. D. (2006). Density-functional theory for charge-transfer: the nature of the N-bands of porphyrins and chlorophylls revealed through CAM-B3LYP, CASPT2, and SAC-CI calculations. *J. Phys. Chem. B* 110, 15624–15632. doi: 10.1021/jp063376t
- Cai, Z.-L., Sendt, K., and Reimers, J. R. (2002). Failure of time-dependent density-functional theory for large extended pi systems. *J. Chem. Phys.* 117, 5543–5549. doi: 10.1063/1.1501131
- Cao, J., Cogdell, R. J., Coker, D. F., Duan, H.-G., Hauer, J., Kleinekathöfer, U., et al. (2020). Quantum biology revisited. *Sci. Adv.* 6:eaz4888. doi: 10.1126/sciadv.aaz4888
- Caricato, M. (2019). Coupled cluster theory with the polarizable continuum model of solvation. *Int. J. Quantum Chem.* 119:e25710. doi: 10.1002/qua.25710
- Casida, M. E. (1995). “Time-dependent density functional response theory for molecules,” in *Recent Advances in Density Functional Methods*, Part 1, ed D. P. Chong (Singapore: World Scientific), 155–192. doi: 10.1142/9789812830586_0005
- Cerezo, J., Aranda, D., Avila Ferrer, F. J., Prampolini, G., and Santoro, F. (2020). Adiabatic-molecular dynamics generalized vertical hessian approach: a mixed quantum classical method to compute electronic spectra of flexible molecules in the condensed phase. *J. Chem. Theory Comput.* 16, 1215–1231. doi: 10.1021/acs.jctc.9b01009
- Chai, J.-D., and Head-Gordon, M. (2008). Long-range corrected hybrid density functionals with damped atom-atom dispersion corrections. *Phys. Chem. Chem. Phys.* 10, 6615–6620. doi: 10.1039/b810189b
- Condon, E. U. (1928). Nuclear motions associated with electron transitions in diatomic molecules. *Phys. Rev.* 32:858. doi: 10.1103/PhysRev.32.858
- den Hartog, F. T. H., Dekker, J. P., van Grondelle, R., and Völker, S. (1998). Spectral distributions of “Trap” pigments in the RC, CP47, and CP47-RC complexes of photosystem II at low temperature: a fluorescence line-narrowing and hole-burning study. *J. Phys. Chem. B* 102, 11007–11016. doi: 10.1021/jp9832793
- Duan, H.-G., Prokhorenko, V. I., Cogdell, R. J., Ashraf, K., Stevens, A. L., Thorwart, M., et al. (2017). Nature does not rely on long-lived electronic quantum coherence for photosynthetic energy transfer. *Proc. Natl. Acad. Sci. U.S.A.* 114, 8493–8498. doi: 10.1073/pnas.1702261114
- Duschinsky, F. (1937). *Acta Physiochim. URSS* 7:551.
- Einstein, A. (1916). Strahlungs-emission und -absorption nach der quantentheorie. *Verhandlungen der Deutschen Physikalischen Gesellschaft* 18, 318–323.
- Fiedor, L., Kania, A., Myśliwa-Kurczel, B., Orzeł Ł., and Stochel, G. (2008). Understanding chlorophylls: central magnesium ion and phytol as structural determinants. *Biochim. Biophys. Acta – Bioenerg.* 1777, 1491–1500. doi: 10.1016/j.bbabi.2008.09.005
- Fiedor, L., Stasiek, M., Myśliwa-Kurczel, B., and Strzałka, K. (2003). Phytol as one of the determinants of chlorophyll interactions in solution. *Photosyn. Res.* 78, 47–57. doi: 10.1023/A:1026042005536
- Frisch, M. J., Trucks, G. W., Schlegel, H. B., Scuseria, G. E., Robb, M. A., Cheeseman, J. R., et al. (2016). *Gaussian 16 Revision C.01*. Wallingford, CT: Gaussian Inc.

- Gillie, J. K., Small, G. J., and Golbeck, J. H. (1989). Nonphotochemical hole burning of the native antenna complex of photosystem I (PSI-200). *J. Phys. Chem.* 93, 1620–1627. doi: 10.1021/j100341a085
- Goerigk, L., and Grimme, S. (2011). A thorough benchmark of density functional methods for general main group thermochemistry, kinetics, and noncovalent interactions. *Phys. Chem. Chem. Phys.* 13, 6670–6688. doi: 10.1039/c0cp02984j
- Gouterman, M., Wagnière, G. H., and Snyder, L. C. (1963). Spectra of porphyrins: part II. Four orbital model. *J. Mol. Spectrosc.* 11, 108–127. doi: 10.1016/0022-2852(63)90011-0
- Grimm, B., Porra, R. J., Rüdiger, W., and Scheer, H. (eds.). (2006). *Chlorophylls and Bacteriochlorophylls*. Dordrecht: Springer. doi: 10.1007/1-4020-4516-6
- Hehre, W. J., Ditchfield, R., and Pople, J. A. (1972). Self-consistent molecular orbital methods. XII. Further extensions of gaussian-type basis sets for use in molecular orbital studies of organic molecules. *J. Chem. Phys.* 56, 2257–2261. doi: 10.1063/1.1677527
- Higashi, M., Kosugi, T., Hayashi, S., and Saito, S. (2014). Theoretical study on excited states of bacteriochlorophyll a in solutions with density functional assessment. *J. Phys. Chem. B* 118, 10906–10918. doi: 10.1021/jp507259g
- Huang, K., Rhys, A., and Mott, N. F. (1950). Theory of light absorption and non-radiative transitions in F-centres. *Proc. Royal Soc. London Series A Math. Phys. Sci.* 204, 406–423. doi: 10.1098/rspa.1950.0184
- Hughes, J. L., Conlon, B., Wydrzynski, T., and Krausz, E. (2010). The assignment of $Q_y(1,0)$ vibrational structure and Q_x for chlorophyll a. *Phys. Procedia* 3, 1591–1599. doi: 10.1016/j.phpro.2010.01.226
- Hughes, J. L., Prince, B. J., Krausz, E., Smith, P. J., Pace, R. J., and Riesen, H. (2004). Highly efficient spectral hole-burning in oxygen-evolving photosystem II preparations. *J. Phys. Chem. B* 108, 10428–10439. doi: 10.1021/jp0492523
- Huo, P., and Coker, D. F. (2010). Iterative linearized density matrix propagation for modelling coherent excitation energy transfer in photosynthetic light harvesting. *J. Chem. Phys.* 133:184108. doi: 10.1063/1.3498901
- Hush, N. S. (1958). Adiabatic rate processes at electrodes. *J. Chem. Phys.* 28:962. doi: 10.1063/1.1744305
- Hush, N. S., and Reimers, J. R. (2000). Solvent effects on transition metal complex spectra. *Chem. Rev.* 100:775. doi: 10.1021/cr980409v
- Jaaniso, R., and Avarmaa, R. (1986). Measurement of the inhomogeneous distribution function and homogeneous spectra of an impurity molecule in a glassy matrix. *Sov. J. Appl. Spectroscopy* 44, 365–370. doi: 10.1007/BF00661051
- Jankowiak, R., Reppert, M., Zazubovich, V., Pieper, J., and Reinot, T. (2011). Site selective and single complex laser-based spectroscopies: a window on excited state electronic structure, excitation energy transfer, and electron-phonon coupling of selected photosynthetic complexes. *Chem. Rev.* 111, 4546–4598. doi: 10.1021/cr100234j
- Kjær, C., Gruber, E., Nielsen, S. B., and Andersen, L. H. (2020). Color tuning of chlorophyll a and b pigments revealed from gas-phase spectroscopy. *Phys. Chem. Chem. Phys.* 22, 20331–20336. doi: 10.1039/D0CP03210G
- Kobayashi, R., and Amos, R. D. (2006). The application of CAM-B3LYP to the charge-transfer band problem of the zincbacteriochlorin-bacteriochlorin complex. *Chem. Phys. Lett.* 420, 106–109. doi: 10.1016/j.cplett.2005.12.040
- Kreisbeck, C., Kramer, T., and Aspuru-Guzik, A. (2014). Scalable high-performance algorithm for the simulation of exciton-dynamics. Application to the light harvesting complex II in the presence of resonant vibrational modes. *J. Chem. Theory Comput.* 10:4045. doi: 10.1021/ct500629s
- Laisk, A., Nedbal, L., and Govindjee. (eds.). (2009). *Photosynthesis In Silico: Understanding Complexity From Molecules to Ecosystems*. Dordrecht: Springer. doi: 10.1007/978-1-4020-9237-4
- Leiger, K., Linnanto, J. M., and Freiberg, A. (2017). Vibronic origin of the Q_y absorption tail of bacteriochlorophyll a verified by fluorescence excitation spectroscopy and quantum chemical simulations. *J. Phys. Chem. Lett.* 8, 4231–4235. doi: 10.1021/acs.jpclett.7b01704
- Magyar, R. J., and Tretiak, S. (2007). Dependence of spurious charge-transfer excited states on orbital exchange in TDDFT: large molecules and clusters. *J. Chem. Theory Comput.* 3, 976–987. doi: 10.1021/ct600282k
- Malý, P., Somsen, O. J. G., Novoderezhkin, V. I., Mančal, T., and van Grondelle, R. (2016). The role of resonant vibrations in electronic energy transfer. *Chemphyschem* 17, 1356–1368. doi: 10.1002/cphc.201500965
- May, V., and Kühn, O. (2008). *Charge and Energy Transfer Dynamics in Molecular Systems*. Weinheim: Wiley.
- Mennucci, B. (2012). Polarizable continuum model. *Wiley Interdiscip. Rev. Comput. Mol. Sci.* 2, 386–404. doi: 10.1002/wcms.1086
- Müh, F., Lindorfer, D., Schmidt am Busch, M., and Renger, T. (2014). Towards a structure-based exciton Hamiltonian for the CP29 antenna of photosystem II. *Phys. Chem. Chem. Phys.* 16, 11848–11863. doi: 10.1039/C3CP55166K
- Pajusalu, M., Rätsep, M., and Freiberg, A. (2014). Temperature dependent electron-phonon coupling in chlorin-doped impurity glass and in photosynthetic FMO protein containing bacteriochlorophyll a. *J. Lumin.* 152, 79–83. doi: 10.1016/j.jlumin.2013.12.011
- Palm, D. M., Agostini, A., Pohland, A.-C., Werwie, M., Jaenicke, E., and Paulsen, H. (2019). Stability of water-soluble chlorophyll protein (WSCP) depends on phytol conformation. *ACS Omega* 4, 7971–7979. doi: 10.1021/acsomega.9b00054
- Peach, M. J. G., Benfield, P., Helgaker, T., and Tozer, D. J. (2008). Excitation energies in density functional theory: an evaluation and a diagnostic test. *J. Chem. Phys.* 128:044118. doi: 10.1063/1.2831900
- Pieper, J., Artene, P., Rätsep, M., Pajusalu, M., and Freiberg, A. (2018). Evaluation of electron-phonon coupling and spectral densities of pigment-protein complexes by line-narrowed optical spectroscopy. *J. Phys. Chem. B* 122, 9289–9301. doi: 10.1021/acs.jpcc.8b05220
- Pieper, J., and Freiberg, A. (2014). “Electron-phonon and exciton-phonon coupling in light-harvesting, insights from line-narrowing spectroscopies,” in *The Biophysics of Photosynthesis*, eds J. Golbeck, and A. van der Est (New York, NY: Springer), 45–77. doi: 10.1007/978-1-4939-1148-6_2
- Purchase, R., and Völker, S. (2009). Spectral hole burning: examples from photosynthesis. *Photosyn. Res.* 101, 245–266. doi: 10.1007/s11220-009-9484-5
- Rätsep, M., Cai, Z.-L., Reimers, J. R., and Freiberg, A. (2011). Demonstration and interpretation of significant asymmetry in the low-resolution and high-resolution Q_y fluorescence and absorption spectra of bacteriochlorophyll a. *J. Chem. Phys.* 134:024506. doi: 10.1063/1.3518685
- Rätsep, M., and Freiberg, A. (2003). Resonant emission from the B870 exciton state and electron-phonon coupling in the LH2 antenna chromoprotein. *Chem. Phys. Lett.* 377, 371–376. doi: 10.1016/S0009-2614(03)01193-X
- Rätsep, M., and Freiberg, A. (2007). Electron-phonon and vibronic couplings in the FMO bacteriochlorophyll a antenna complex studied by difference fluorescence line narrowing. *J. Lumin.* 127, 251–259. doi: 10.1016/j.jlumin.2007.02.053
- Rätsep, M., Linnanto, J., and Freiberg, A. (2009a). Mirror symmetry and vibrational structure in optical spectra of chlorophyll a. *J. Chem. Phys.* 130:194501. doi: 10.1063/1.3125183
- Rätsep, M., Linnanto, J. M., and Freiberg, A. (2019a). Higher order vibronic sidebands of chlorophyll a and bacteriochlorophyll a for enhanced excitation energy transfer and light harvesting. *J. Phys. Chem. B* 123, 7149–7156. doi: 10.1021/acs.jpcc.9b06843
- Rätsep, M., Linnanto, J. M., Muru, R., Biczysko, M., Reimers, J. R., and Freiberg, A. (2019b). Absorption-emission symmetry breaking and the different origins of vibrational structures of the 1Q_y and 1Q_x electronic transitions of pheophytin a. *J. Chem. Phys.* 151:165102. doi: 10.1063/1.5116265
- Rätsep, M., Pajusalu, M., and Freiberg, A. (2009b). Wavelength-dependent electron-phonon coupling in impurity glasses. *Chem. Phys. Lett.* 479, 140–143. doi: 10.1016/j.cplett.2009.07.094
- Rätsep, M., Wu, H. M., Hayes, J. M., and Small, G. J. (1998). Stark hole-burning spectroscopy of a photosynthetic complex: LH2 of purple bacteria. *Spectrochim. Acta A* 54, 1279–1289. doi: 10.1016/S1386-1425(98)0076-6
- Rebane, K. K. (1970). *Impurity Spectra of Solids*. New York, NY: Plenum Press.
- Rebane, K. K., and Avarmaa, R. A. (1982). Sharp line vibronic spectra of chlorophyll and its derivatives in solid solutions. *Chem. Phys.* 68, 191–200. doi: 10.1016/0301-0104(82)85094-5
- Reimers, J. R. (2001). A practical method for the use of curvilinear coordinates in calculations of normal-mode projected displacements and Duschinsky rotation matrices for large molecules. *J. Chem. Phys.* 115, 9103–9109. doi: 10.1063/1.1412875
- Reimers, J. R., Cai, Z.-L., Kobayashi, R., Rätsep, M., Freiberg, A., and Krausz, E. (2013). Assignment of the Q-bands of the chlorophylls: coherence loss via $Q_x - Q_y$ mixing. *Sci. Rep.* 3:2761. doi: 10.1038/srep02761

- Reimers, J. R., Cai, Z.-L., Kobayashi, R., Rätsep, M., Freiberg, A., and Krausz, E. (2014). Formation of water-chlorophyll clusters in dilute samples of chlorophyll-a in ether at low temperature. *Phys. Chem. Chem. Phys.* 16, 2323–2330. doi: 10.1039/C3CP53729C
- Reimers, J. R., and Krausz, E. (2014). An analytical data inversion method for magnetic circular dichroism spectra dominated by the “B-term”. *Phys. Chem. Chem. Phys.* 16, 2315–2322. doi: 10.1039/C3CP53730G
- Ren, J., Shuai, Z., and Kin-Lic Chan, G. (2018). Time-dependent density matrix renormalization group algorithms for nearly exact absorption and fluorescence spectra of molecular aggregates at both zero and finite temperature. *J. Chem. Theory Comput.* 14, 5027–5039. doi: 10.1021/acs.jctc.8b00628
- Renge, I., Mauring, K., and Avarmaa, R. (1987). Site-selection optical spectra of bacteriochlorophyll and bacteriopheophytin in frozen solutions. *J. Lumin.* 37, 207–214. doi: 10.1016/0022-2313(87)90161-X
- Renge, I., Rätsep, M., and Freiberg, A. (2011). Intermolecular repulsive–dispersive potentials explain properties of impurity spectra in soft solids. *J. Lumin.* 131, 262–265. doi: 10.1016/j.jlumin.2010.10.008
- Renger, T., Voigt, J., May, V., and Kühn, O. (1996). Dissipative exciton motion in a chlorophyll a/b dimer of the light harvesting complex of photosystem II: simulation of pump - probe spectra. *J. Phys. Chem.* 100, 15654–15662. doi: 10.1021/jp960486z
- Rivera, E., Montemayor, D., Masia, M., and Coker, D. F. (2013). Influence of site-dependent pigment-protein interactions on excitation energy transfer in photosynthetic light harvesting. *J. Phys. Chem. B* 117, 5510–5521. doi: 10.1021/jp4011586
- Romero, E., Augulis, R., Novoderezhkin, V. I., Ferretti, M., Thieme, J., Zigmantas, D., et al. (2014). Quantum coherence in photosynthesis for efficient solar-energy conversion. *Nat. Phys.* 10, 676–682. doi: 10.1038/nphys3017
- Shafizadeh, N., Ha-Thi, M. H., Soep, B., Gaveau, M. A., Piuzzi, F., and Pothier, C. (2011). Spectral characterization in a supersonic beam of neutral chlorophyll a evaporated from spinach leaves. *J. Chem. Phys.* 135:114303. doi: 10.1063/1.3637048
- Sild, O., and Haller, K. (eds.). (1988). *Zero-Phonon Lines And Spectral Hole Burning in Spectroscopy and Photochemistry*. Berlin: Springer. doi: 10.1007/978-3-642-73638-4
- Sirohiwal, A., Berraud-Pache, R., Neese, F., Izsák, R., and Pantazis, D. A. (2020). Accurate computation of the absorption spectrum of chlorophyll a with pair natural orbital coupled cluster methods. *J. Phys. Chem. B* 124, 8761–8771. doi: 10.1021/acs.jpcc.0c05761
- Skyner, R. E., McDonagh, J. L., Groom, C. R., van Mourik, T., and Mitchell, J. B. O. (2015). A review of methods for the calculation of solution free energies and the modelling of systems in solution. *Phys. Chem. Chem. Phys.* 17, 6174–6191. doi: 10.1039/C5CP00288E
- Tomasi, J. (2011). Selected features of the polarizable continuum model for the representation of solvation. *Wiley Interdiscip. Rev. Comput. Mol. Sci.* 1, 855–867. doi: 10.1002/wcms.54
- Tomasi, J., Mennucci, B., and Cammi, R. (2005). Quantum mechanical continuum solvation models. *Chem. Rev.* 105, 2999–3093. doi: 10.1021/cr9904009
- Tomasi, S., and Kassal, I. (2020). Classification of coherent enhancements of light-harvesting processes. *J. Phys. Chem. Lett.* 11, 2348–2355. doi: 10.1021/acs.jpcllett.9b03490
- Umetsu, M., Wang, Z.-Y., Kobayashi, M., and Nozawa, T. (1999). Interaction of photosynthetic pigments with various organic solvents: magnetic circular dichroism approach and application to chlorosomes. *Biochim. Biophys. Acta – Bioenerg.* 1410, 19–31. doi: 10.1016/S0005-2728(98)00170-4
- van Grondelle, R., Dekker, J. P., Gillbro, T., and Sundström, V. (1994). Energy transfer and trapping in photosynthesis. *Biochim. Biophys. Acta* 1187, 1–65. doi: 10.1016/0005-2728(94)90166-X
- Wilson, E. B., Decius, J. C., and Cross, P. C. (1955). *Molecular Vibrations: The Theory of Infrared and Raman Vibrational Spectra*. New York, NY: McGraw-Hill Book Company. doi: 10.1149/1.2430134
- Yanai, T., Tew, D. P., and Handy, N. C. (2004). A new hybrid exchange-correlation functional using the Coulomb-attenuating method (CAM-B3LYP). *Chem. Phys. Lett.* 393, 51–57. doi: 10.1016/j.cplett.2004.06.011
- Yu, H. S., He, X., Li, S. L., and Truhlar, D. G. (2016). MN15: a Kohn–Sham global-hybrid exchange–correlation density functional with broad accuracy for multi-reference and single-reference systems and noncovalent interactions. *Chem. Sci.* 7, 5032–5051. doi: 10.1039/C6SC00705H
- Zazubovich, V., Tibe, I., and Small, G. J. (2001). Bacteriochlorophyll a Frank-Condon factors for the S_0 - $S_1(Q_y)$ transition. *J. Phys. Chem. B* 105, 12410–12417. doi: 10.1021/jp012804m
- Zuehlsdorff, T. J., and Isborn, C. M. (2018). Combining the ensemble and Franck-Condon approaches for calculating spectral shapes of molecules in solution. *J. Chem. Phys.* 148:024110. doi: 10.1063/1.5006043

Conflict of Interest: The authors declare that the research was conducted in the absence of any commercial or financial relationships that could be construed as a potential conflict of interest.

Copyright © 2020 Reimers, Rätsep and Freiberg. This is an open-access article distributed under the terms of the Creative Commons Attribution License (CC BY). The use, distribution or reproduction in other forums is permitted, provided the original author(s) and the copyright owner(s) are credited and that the original publication in this journal is cited, in accordance with accepted academic practice. No use, distribution or reproduction is permitted which does not comply with these terms.